COUPLED FLOW-GEOMECHANICS NUMERICAL INVESTIGATION OF MICROEARTHQUAKES AND PLANAR FRACTURE PROPAGATION IN THE BARNETT SHALE

A Thesis

by

EDUARDO MARTINEZ RODRIGUEZ

Submitted to the Office of Graduate and Professional Studies of
Texas A&M University
in partial fulfillment of the requirements for the degree of

MASTER OF SCIENCE

Chair of Committee,	Jihoon Kim
Committee Members,	Zenon Medina-Cetina
	Eduardo Gildin
Head of Department,	A. Daniel Hill

December 2017

Major Subject: Petroleum Engineering

ABSTRACT

The purpose of this study is to investigate the effects of hydraulic fracturing stimulation for development of shale gas reservoirs. Particularly, the study considers the vertical planar fracture propagation and induced seismicity during hydraulic fracturing operations in the Barnett Shale.

To this end, a sequentially implicit coupled-flow-geomechanics-geophysical simulator is used to generate a realistic model and to study the effects and potential issues surrounding hydraulic fracturing stimulating vertical and horizontal wells in the Barnett Shale. In addition, a sensitivity analysis is performed on the model to determine how the uncertainty of the model outputs can be apportioned to different sources of uncertainty in its inputs.

From the results of the model combined with the literature, we obtain stable fracture propagation, having the limited vertical extent of the fractures. Furthermore, the model suggests that vertical extent of fractures is limited due to rock strength heterogeneity and variations of the stress field, while failure around cementing wells might be possible. Additionally, the magnitude of modelled the micro-earthquakes generated during hydraulic fracturing stimulation were not large enough to warrant safety concerns regarding seismicity, unless faults exist nearby.

Finally, based on the outputs of the model, it is possible to couple a sequential flow-geomechanics simulator to model micro-earthquakes, fracture propagation, and stimulated reservoir area.

DEDICATION

I would like to dedicate this thesis to my wife Victoria, my brother Diego and my parents Ramon and Tina. They have encouraged and supported me throughout this process. My success is their success. A special loving dedication to my grandparents Manolo, Dario and Concepcion for all of their sacrifices.

ACKNOWLEDGEMENTS

I would like to thank my committee chair, Dr. Kim, and my committee members, Dr. Medina-Cetina, and Dr. Gildin for their guidance and support throughout the course of this research.

I would also like to thank all my friends at Harold Vance Department faculty and the amazing staff for making my time at Texas A&M University a great learning experience.

I also want to extend my gratitude to RPSEA and Texas A&M University for providing the funding that allowed me to fulfil this research.

Finally, I would like to thank my research colleague, Jaeyoung Park, for his constant support throughout my thesis.

CONTRIBUTORS AND FUNDING SOURCES

This work was supervised by a thesis committee consisting of Professor Jihoon Kim and Eduardo Gildin of the Harold Vance Department of Petroleum Engineering and professor Zenon Medina-Cetina of the Zachry Department of Civil Engineering.

The reservoir simulator used in Chapter 5 was provided by Professor Jihoon Kim and developed in the Lawrence Berkeley National Laboratory.

All work for the thesis (or) dissertation was completed independently by the student.

This graduate study was supported by the start-up fund from Texas A&M University, and also by RPSEA (Contract No. 10122-42) through the Ultra-Deepwater and Unconventional Natural Gas and Other Petroleum Resources Research and Development Program as authorized by the US Energy Policy Act (EPAct) of 2005.

NOMENCLATURE

c_f	Formation Compressibility
ϕ	Porosity/True Porosity
V_ϕ	Pore or void space volume of the rock
p	Pressure
c_r	Rock Compressibility
$\boldsymbol{\sigma}$	Total Stress Tensor
ρ_b	Bulk Density
ρ_f	Fluid Density
$\mathbf{g}$	Gravity
Div	Divergence Operator
$\boldsymbol{u}$	Displacement Vector
Grad	Gradient Operator
$\boldsymbol{\varepsilon}$	Strain
$\mathbf{C}_{\mathrm{dr}}$	Rank-4 drained elasticity tensor
$\mathbf{1}$	Rank-2 identity tensor
p	Fluid pressure
m	Fluid mass per unit bulk volume
M	Biot Modulus
ε_v	Volumetric Strain
b	Biot coefficient

K_s	Bulk modulus of the solid grain
K_{dr}	Drained bulk modulus
$\mathbf{e}$	Deviatoric portion of strain poroelastic equation
$\boldsymbol{s}$	Deviatoric portion of stress poroelastic equation
σ_v	Volumetric Stress
$\mathbf{w}$	Fluid mass flux
f	Volumetric source term
$\mathbf{v}$	Fluid velocity relative to the solid phase
$\mathbf{k_p}$	Positive-definite absolute-permeability tensor
μ	Fluid viscosity
$\frac{dE}{dt}$	Change in internal energy with respect to moving solid skeleton
e	Internal energy with respect to moving skeleton
$\mathbf{q}$	Heat flux
S	Total entropy
s	Internal entropy per unit mass of phase
$\mathbf{F}$	Body force
r	Heat conduction
Ψ	Helmholtz free energy
T	Temperature
g	Gibb's potential
Φ_1	Intrinsic dissipation

Φ_2	Thermal dissipation
$\mathrm{k_c}$	Thermal conductivity
Φ_3	Dissipation due to mass transport
$\mathbf{k}_p$	Fourth order positive define permeability tensor
$\mathbf{C}_{ud}$	Undrained bulk moduli
$\mathbf{C}_{dr}$	Drained bulk moduli
Q_f	Volume flow rate per unit plate width
Δh	Head gradient
f_r	Friction factor
b_f	Apparent physical aperture
k_f	Fracture permeability
$k_{f,0}$	Reference permeability of the fracture
$\mathbf{t}_s$	Shear traction
t_n	Normal traction
T_c	Tensile Strength of the material
M_{pq}	Seismic moment tensor
m_{pq}	Moment density tensor
M_0	Seismic moment
M_w	Moment magnitude
Δu_{rs}	Nodal displacement change
c_{pqrs}	Stiffness Tensor

TABLE OF CONTENTS

Page

LIST OF FIGURES

Page

LIST OF TABLES

Page

LIST OF EQUATIONS

Page

1. INTRODUCTION

Hydraulic fracturing is a formation stimulation practice used to create additional permeability in a producing formation to facilitate the migration of fluids to the wellbore for purposes of production. The process has come to the forefront of the oil and gas industry for its ability to unlock reserves from traditionally limited reservoirs by producing them at economic levels.

Hydraulic fracturing stimulation involves pumping large amounts of sand laden water into the target shale zone. Fluids pumped into the shale creates fractures or openings through which the sand flows, at the same time the sand acts to prop open the fractures that have been created. Once the pumping of fluids has stopped the sand remains in-place allowing fluids (both gas and water) to flow back to the wellbore. This completion jobs have been refined and modernized through recent years which have converted them into sophisticated processes that cost millions of dollars.

However, due to the increase of hydraulic fracturing activity within the United States, and the media attention that fracking has captured in recent years, public concern about impacts of hydraulic fracturing has become an issue when discussing shale development. This has added an extra layer of complexity for oil and gas operators and the need for studies on potential negative impacts of hydraulic fracturing.

The purpose of this thesis, then, is to: (1) Study the potential negative effects of hydraulic fracturing stimulation surrounding seismicity (2) Provide insights into which operating conditions have higher risk (3) Use a sequentially coupled flow-

geomechanics-geophysical simulator for all simulations (4) Study the uncertainty of the model outputs in relation to the uncertainty in its inputs.

In order to reach these objectives, an extensive literature review regarding hydraulic fracturing in the Barnett Shale was combined with several coupled flow-geomechanical-geophysical simulations of both vertical and horizontal wells. The simulator outputs would then be processed to generate fracture propagation visualization and earthquake moment magnitudes to analyze potential risks. Finally, a sensitivity analysis would be carried out on the model to properly quantify the relationship between uncertainty in the inputs and outputs.

Current commercial hydraulic fracturing simulators employee loosely couple schemes that are unable to accurately predict geomechanics responses to fluid injection. The majority of commercial available software typically do not calculate the variations at specific points within the fracture. Instead, the effects are integrated into functional coefficients of the governing differential equations, which greatly simplifies the calculations of fracture dimensions. This simplification emphasizes calculation speed in detriment of full domain accuracy, but it is generally accepted as the overall differences are low and operators tend to emphasized completion design flexibility over simulation accuracy.

However, when dealing with potential public safety issues, such as seismicity generation, it is important to obtain accurate solutions to properly evaluate risk associated with fracture propagation within a reservoir. Furthermore, from the literature review of this thesis, no fracture simulation software have been coupled to a geophysical

model to calculate generated earthquakes magnitude during hydraulic fracturing stimulation treatments.

Therefore, a comprehensive analysis using a coupled flow-geomechanics-geophysical simulator is needed to properly assess the seismicity risks derived from hydraulic fracturing.

As a result, this thesis employs a fixed stress sequential coupled scheme, which means that the flow problem is solved first and then the solutions from the flow simulation are used as inputs for the geomechanics simulator. After, the porosity corrections is used to adjust the inconsistency between the porosity computed from the conventional flow simulation and the strains from the mechanical simulation. This approach guarantees conversion and it is unconditionally stable at every time step of the simulation. By employing this solution scheme for all numerical simulations, an accurate solution is calculated for every point within the simulation domain. This employed approach emphasizes accuracy over calculation time, which in turn are used to calculate fracture propagation, but it also allows to output the displacement at each domain node for every time step. This information is used to compute and calculate the earthquake moment magnitude *a priori*. Additionally, the simulations done on this research take place in the Barnett shale to test the sequential coupled flow-geomechanics-geophysical simulator for operational accuracy by using it under shale reservoir parameters obtained from previous studies and literature.

1.1 Literature Review

1.1.1 Coupled Processes and Simulators

The transport of heat and fluids in soils and rocks can be affected by significant coupling between thermal, hydrological, mechanical, and chemical (THMC) processes. Since hydrocarbon reservoir depletion is a complex problem that derives into non-linear irreversible relationships between flow and geomechanics, flow may not only depend in a direct and linear manner on its constitutive equations, but also on non-conjugated forces (geomechanics) that are present (Bear 2013).

Coupled processes, and in specific coupled flow-geomechanics processes, have gained recent traction in petroleum engineering due to its ability to accurately assess petroleum reservoir geomechanics. A high number of coupled flow-geomechanics simulators for petroleum reservoir have recently emerged, and coupling schemes have been added to traditional commercial reservoir software.

However, conventional reservoir simulation has oversimplified reservoir mechanical effects by only using rock compressibility, taken as a constant coefficient or a simple function of porosity that cannot quantify the deformation and stress fields accurately (Kim 2011). Later efforts to increase this relationship accuracy realized that these compressibilities are not constant but tend to be combination of factors such as pressure and formation geology, but It was not until the introduction of poroelasticity and poroelastoplasticity theories by Olivier Coussy (1995) that this particular area of reservoir engineering obtained a reliable physical model and framework over which to develop.

Coussy developed the framework for mechanics of porous continua by accurately employing the concept of porous medium to reservoir engineering. The underlying idea is the representation of a saturated porous medium as the superposition, in time and space, of two continua; the first representing the skeleton, the second the fluid (Bear 2013). Additionally, Coussy was able to accurately describe his theory of Mechanics of Porous Continua without requiring separate consideration of each phase, making it consistently macroscopic in its foundation (Coussy 1995). His analytical coupled equations opened up several areas of research specialized in the effects of porous medium deformation when subjected to various external actions and physical phenomena. Many disciplines, including reservoir engineering, have benefited greatly from Coussy's work, and the numerical application of his analytical constitutive equations created two main solution strategies: fully coupled and sequential implicit methods.

- Fully coupled methods (monolithic schemes): The coupled problem is solved simultaneously in a time-stepping algorithm, where an implicit scheme is typically adopted. This approach typically achieves unconditional stability and convergence when the coupled problem is well-posed (Kim et al 2011)
- Sequential implicit methods: The coupled problem is partitioned and each sub-problem is solved sequentially. Each sub-problem (or part) can take a different implicit time-stepping algorithm. The partitioning allows for the use of existing robust simulators for the sub-problems, producing smaller systems of equations to be solved than the fully coupled methods (Kim et al 2011).

Traditionally, fully coupled methods have been used in several coupled flow and geomechanics problems because they guarantee stability and convergence, necessary conditions for an accurate solutions. However, fully coupled methods require a unified flow-mechanics simulator, intense computational cost, and complicated code management, leading to large systems to solve. Conversely, sequential methods provide flexibility and efficient code management (Kim et al 2011).

Sequential methods in reservoir geomechanics use the so-called porosity correction, which sequentially corrects the inconsistency between the porosity computed from the conventional flow simulation and the strains from the mechanical simulation and can be considered as a predictor–corrector approach (Kim et al 2013). However, the main concern with sequential methods is that they do not necessarily guarantee unconditional stability and convergence even though the uncoupled sub-problems are unconditionally stable and convergent (Kim et al 2011). Several authors have proposed and investigated the stability and convergence of sequential methods, which depends greatly on what problem is solved first: flow or geomechanics.

Kim (2011) performed stability and convergence analyses for two sequential methods which solve the flow problem first, namely fixed-strain and fixed-stress splits. Kim found that the fixed-strain split is conditionally stable and oscillatory while the fixed-stress split is unconditionally stable. **As a result, the fixed stress coupled scheme is employed to solve coupled flow geomechanics throughout this thesis**.

1.1.2 Barnett Shale

The Barnett shale reservoir is located in the Forth-Worth Basin of northern Texas. The reservoir rock itself is a Mississippian age organic-rich shale, as the depositional system of the basin contained type I and II kerogen. Rock composition changes across the different fields and within the reservoir section, as the shale layer lays conformably overlain by Pennsylvanian Marble Falls Limestone. In the eastern part of the basin, the upper quarter of the Barnett Shale is separated from the lower Barnett Shale by the Forestburg limestone.

Additionally, the Barnett formation is characterized for having generally high silica content, relatively low clay content, and significant organic carbon content more accurately described as a siliceous mudstone than a shale (Lockus and Ruppel 2007). Furthermore, depths of the formation for the productive regions range from less than 4000 feet in the west to more than 8500 feet in the east, with net thickness increasing from 200 feet to 500 feet moving from the west to the east in the basin (Zhao et al, 2007).

The potential of the Barnett shale as a productive natural gas reservoir was discovered in 1981 by Mitchell Energy (Martineau, 2007). In a recent study conducted by the Bureau of Economic Geology (BEG), the Barnett shale forecasted a cumulative 44 trillion cubic feet (TCF) of recoverable reserves, with annual production declining in a predictable curve from a peak of 2 Tcf per year to about 900 billion cubic feet (Bcf) per year by 2030. Additionally, current regional gains in business activity and tax receipts related to the Barnett Shale include $11.8 billion in gross product per year and

more than 107,650 permanent jobs generating annual tax receipts to the local government entities and the State of approximately $480.6 million and $644.7 million, respectively (Perryman Report: Barnett Shale n.d.).

However, despite its abundant known resources and economic potential, past drilling and completions technologies could not turn the Barnett shale resources into economic production. It was not until in 1997 when Mitchell energy began to fracture wells using slick-water fracturing fluid that potential for viable economic wells was realized. The success of slick-water fracturing, and the subsequent development of multi-stage fracturing in horizontal wells, led to a rapid growth in development over the last 15 years.

The Barnett shale was one of the first major unconventional resources exploited in the United States, and at its peak production year (2012) it produced approximately 5.7 Bcf of gas and a combined 25 mmbbl of condensate and oil (EIA 2013). Although it is no longer the main economic driver of shale hydrocarbon activities within the United States, the Barnett shale development importance cannot be overstated. To this day, the Barnett shale still has seen the most development of any gas shale reservoir in the world. Furthermore, as its basins were depleted, the information gained from its development provided the initial technology template for developing other shale plays in the United States, starting the shale revolution of the last decade.

1.1.3 Hydraulic Fracturing

Hydraulic fracturing is a formation stimulation practice used to create additional permeability in a producing formation. By creating additional permeability, hydraulic fracturing facilitates the migration of fluids to the wellbore for purposes of production. Hydraulic fracturing can be used to overcome barriers to the flow of fluids, one of the primary reasons development of gas shales has traditionally been limited. Barriers may include naturally low permeability common in shale formations or reduced permeability resulting from near wellbore permeability impairment caused during drilling activities. While aspects of hydraulic fracturing have been changing and maturing, this technology has been utilized by industry to increase production to support the increasing demand for energy for over 60 years (Arthur et al 2009).

The hydraulic fracturing process used in oil and gas shale reservoirs consist of pumping barrels of water mixed with sand into the target formation. The fluid injected into the shale overpressures the formation and creates fracture through which the sand flows. This sand props the fracture open and allows hydrocarbons and water to flow back to the wellbore.

Given the substantial costs of hydraulic treatment, there is a special emphasis on effective treatment design. Data, such as direction and magnitude of principal stresses, is collected from the reservoir to predict basin behavior during and after injection of proppant fluid. This data is used as input on fracture simulators to evaluate and assess fracture treatments in a controlled setting. Additionally, by incorporating data obtained during hydraulic treatments, fracturing designs are constantly being refined to optimize

fracture networking and to maximize gas production, while ensuring that fracture development is confined to the target formation (Arthur et al 2009).

Hydraulic fracturing treatments are composed of multiple steps of different duration and cost. The fracturing steps are sub-divided because it is usually not possible to maintain a downhole pressure sufficient to stimulate the entire length of a lateral in a single stimulation event. A one stage hydraulic fracture treatment might entail rig-up, re-up, perforation, isolation of fracture stage, fresh water flush, acid flush, spacer, shut-in, clean fluid pad injection, proppant sub-stages, and a final flush.

1.1.4 Micro Earthquakes (MEQ)

Despite hydraulic fracturing basic steps (as described in section 1.1.3), the processes by which hydraulic fracturing leads to an interconnected/permeable fracture network are still poorly understood. The development of successful hydraulic fracturing methods is too often a trial and error process and our ability to even quantify the success of hydraulic fracturing is still in doubt. In addition, the relationship between stress change, fracturing, and permeable volume creation had been underexplored until the introduction of the more rigorous coupled schemes.

One of the major challenges for operators when developing specific gas shale fields is to estimate the success of stimulation soon after, or even during, hydraulic fracturing. However, with the presented framework of this research, a better *a priori* understanding of the fracture process can be used to make better and safer engineering decisions.

Triggered seismicity occurs as injected fluids reduce the normal fault stress, which releases the stored fault stress and triggers a seismic event. This induced seismicity is identified by spatial proximity and multiple temporal correlations between fluid injection parameters and earthquake occurrence (McClure et al 2016), but hydraulic treatment earthquakes are typically very small.

Additionally, hydraulic treatments are monitored by operators and service companies. Monitoring has been integrated as a major part of the hydraulic fracturing process because surveillance technologies can define the success and orientation of the fractures created during a stimulation process. MEQ monitoring has led to important information with regards to frac treatments and micro-seismicity, like the fact that hydraulic fracturing is associated with fault activation. For this thesis, MEQs are studied using the node displacement information from the output of the coupled simulator and transforming those displacements into a moment magnitude scale (Dahm and Kruger 2014).

1.1.4.1 Micro-Earthquakes and Hydraulic Fracturing

The accepted mechanism for triggered seismicity for both hydraulic fracturing and injection of fluids at depth is the diffusion of pore pressure and its subsequent increase, effectively reducing the normal fault stress, releasing stored fault stress and triggering earthquakes (Hsieh and Bredehoeft, 1981).

Microearthquakes are typically studied using moment tensor equations derived by Aki and Richards (2002). Moment tensors provide the general theoretical framework

to describe seismic sources based on generalized force couples. The moment tensor description is not restricted to earthquake sources, but covers also other types of seismic sources such as mixed mode ruptures driven by fluid and gas injections (hydraulic fracturing) (Dahm and Kruger 2014)

In this context, induced seismicity from fluid injection at depth is often identified by spatial proximity and multiple temporal correlations between fluid injection parameters and earthquake occurrence. Generally, earthquakes associated with hydraulic fracturing are very small microseismic events with reported magnitudes in the range of −3.0 to −0.5 (Dahm and Kruger 2014). A seismicity study conducted in Oklahoma determined that earthquakes occurred in close proximity (< 5 km) to injection wells (Holland 2013), with an apparent correlation between injection volume and earthquake occurrence (De Pater and Baisch 2011).

However, there is uncertainty in absolute earthquake locations due to a lack of seismic stations at close proximity, which impedes a full evaluation and adds uncertainty to the correlations between hydraulic fracturing and seismicity (Holland 2013). It is important to minimize any earthquake location uncertainty, as accurate MEQs whereabouts could potentially help us learn more about subsurface properties, stresses, strength of faults, fracture propagation, fluid flow, pressure diffusion, triggering mechanisms, and long-term fault and earthquake behaviors of the stable continent (Holland 2013). It may also be possible to identify what criteria may affect the likelihood of induced earthquakes and provide oil and gas operators the ability to mitigate the possibility of triggering a damaging earthquake.

1.1.4.2 Fracture Monitoring

Hydraulic fracturing stimulations are monitored continuously by operators and service companies to evaluate and document the events of the hydraulic fracturing treatments. Monitoring of fracture treatments includes tracking the process with wellhead and downhole pressures, pumping rates, fracturing fluid/slurry density measurements, additive volume, water volume, and ensuring that equipment is functioning properly (Arthur et al 2009).

Hydraulic fracturing monitoring has become a major part of the process because of its ability to map where fracturing occurs during a stimulation treatment and includes such techniques as microseismic fracture mapping, and tilt meter measurements (Arthur, et al, 2008) in real time. Additionally, these technologies can be used to define the success and orientation of the fractures created during a stimulation process.

Microearthquakes (MEQs) in this thesis are studied using the information compiled from the output of the coupled simulator. By using the displacement of the fracture nodes at different times, it is possible to compute the fracture area and moment density tensor, which in turn are used to calculate the seismic moment. Once the seismic moment is calculated, it can be transformed into the moment magnitude scale (Aki and Richards 2002) and compared across the different cases.

1.1.4.3 Public Concern

Due to the increased number of wells drilled and the media attention that hydraulic fracturing has captured in recent years, public concern about health and safety

impact of hydraulic fracturing has become a predominant issue when discussing shale development, and impacts induced by hydraulic fracturing are constantly examined.

There are numerous studies regarding concerns of fracking, but the predominant argument against it is the possibility of triggered seismicity. Hydraulic fracturing operations have been documented to generate seismicity activity nearby shale wells (Holland 2013; Maxwell et al 2009; Warpinski, 2009). This is because during hydraulic fracturing a large planar fracture is created in a direction perpendicular to the minimum horizontal stress. In addition to this, a significant number of shear failures (micro-earthquakes) are generated in the surrounding intact reservoir rock (Vermylen 2011). Additionally, as water leaks off from the main hydraulic fracture plane into the surrounding rock, the increased pore pressure leads to shear slip on preexisting planes of weakness that are well-oriented for slip in the existing stress state. This slip produced by hydraulic fracturing creates micro-seismic events of lower magnitude that have been traced through micro-seismic monitoring.

These MEQ (micro-earthquake) events tend to be of low magnitude, so they do not represent a hazard to the general public. In a recently documented case, small earthquakes of M 2.3 and smaller were observed associated with hydraulic fracturing of the Bowland Shale in the United Kingdom (De Pater and Baisch, 2011). Furthermore, an earthquake of magnitude M 2.9 was registered at the Eola-Robberson field during hydraulic fracturing operations in South Central Oklahoma (Holland 2013).

Even though the average micro-earthquake generated from hydraulic fracturing does not represent a threat to public safety, isolated cases such as the one in the Bowland

Shale in combination with the shocking nature of earthquakes have negatively shaped public opinion. In order to restore trust, it is important to conduct accurate and reliable research into the seismicity implications of hydraulic fracturing operations.

1.2 Outline

This thesis has been split into five different chapters. In Chapter 2, we explain the general framework for nonlinear formulations of coupled flow and geomechanics, and we describe the constitutive relations consistent with Biot's theory Biot (1941). The formulation integrates the approaches proposed by several researchers and it is thermodynamically consistent. Additionally, failure criteria, seismicity and permeability equations are defined and explained on this chapter. In Chapter 3, aspects related to numerical modelling are explained and defined including: discretization, fracture propagation, solution scheme, simulators, and reservoir domain. In Chapter 4, we cover the numerical results of modelling planar fracture propagation and MEQs during hydraulic fracturing stimulation of the Barnett shale, for both vertical and horizontal wells, as well as including a sensitivity analysis of the simulator inputs. Finally, in Chapter 5, we summarize our findings.

2. MATHEMATICAL DESCRIPTION

This thesis follows the coupling constitutive equations for single phase flow slightly compressible fluid derived by Biot (1941), Geertsma (1957), and Biot and Willis (1957). They also proposed appropriate laboratory tests that can determine the various coupling coefficients.Coussy (1995) and Coussy et al. (1998) were the first authors to provide thermodynamically consistent constitutive relations, so their derivation is widely accepted as the basis for thermodynamically consistent equations and it is therefore used throughout this thesis. The purpose of this chapter, then, is to describe the full formulation and provide expressions of the constitutive and governing relations of coupled single phase flow and geomechanics. These relations will in turn be used by a planar fracture and MEQ simulator during hydraulic fracturing stimulation. In addition to the constitutive equations by Coussy, this chapter goes over other aspects of the coupled simulator such as permeability treatment, failure criteria and micro-earthquakes (MEQs) formulation and calculation.

2.1 Governing Equations

In addition to using Coussy's formulation, this thesis simulator was developed assuming isothermal single-phase flow, isotropic geo-material, no stress-dependence of flow properties, and infinitesimal transformation.

The physical model is based on poroelasticity and poroelastoplasticity theories (Coussy 1995). The governing equations come from the **mass conservation and linear-**

momentum balance equations assuming quasi-static behavior. Under the quasi-static assumption for porous media displacements, the governing equation for mechanical deformation of the solid fluid system can be written as:

$$\mathrm{Div}(\boldsymbol{\sigma}) + \rho_b \mathbf{g} = 0$$

Equation 1. Linear momentum balance equation

where $\boldsymbol{\sigma}$ is the total stress tensor, $\rho_b = \phi\rho_f + (1-\phi)\rho_s$ is the bulk density, ρ_f is the fluid density, ρ_s is the density of the solid phase, ϕ is the true porosity, $\mathbf{g}$ is the gravity vector, and Div is the divergence operator. True porosity is defined as the ratio of the pore volume to the bulk volume in the deformed configuration.

The infinitesimal transformation assumption is used to allow the strain, $\boldsymbol{\varepsilon}$, to be a linearized strain tensor of the displacement vector, $\boldsymbol{u}$, where Grad is the gradient operator.

$$\boldsymbol{\varepsilon} = \mathrm{Grad}^{\mathrm{s}}\boldsymbol{u} = \frac{\mathbf{1}}{\mathbf{2}}(\mathrm{Grad}\,\boldsymbol{u} + \mathrm{Grad}^{\mathrm{t}}\boldsymbol{u})$$

Equation 2. Linearize strain tensor in terms of displacement

Additionally, it is necessary to specify a stress-strain relation for the mechanical behavior of the porous medium, and the poroelasticity equations are given as

$$\boldsymbol{\sigma} - \boldsymbol{\sigma_0} = \mathbf{C}_{\mathrm{dr}} : \boldsymbol{\varepsilon} - b(p - p_0)\mathbf{1}$$

Equation 3. Stress poroelasticity equation

$$\frac{1}{\rho_{f,0}}(m - m_0) = b\varepsilon_v + \frac{1}{M}(p - p_0)$$

Equation 4. Strain poroelasticity equation

where $\mathbf{C}_{\mathrm{dr}}$ is the rank-4 drained elasticity tensor, $\mathbf{1}$ is the rank-2 identity tensor, p is fluid pressure, m is fluid mass per unit bulk volume, M is the Biot modulus, ε_v is the volumetric strain, and b is the Biot coefficient. The subscript 0 refers to the initial state. The Biot modulus M, is defined in terms of true porosity ϕ_0, fluid compressibility c_f, Biot coefficient b, and bulk modulus of the solid grain K_s.

$$\frac{1}{M} = \phi_0 c_f + \frac{b - \phi_0}{K_s}$$

Equation 5. Biot modulus

In this thesis, tensile stress is positive. Changes in total stress and fluid pressure are related to changes in strain and fluid content. Similarly, the Biot coefficient b can be defined in terms of bulk modulus of the solid grain K_s, and drained bulk modulus K_{dr}.

$$b = 1 - \frac{K_{dr}}{K_s}$$

Equation 6. Biot coefficient

Both of these coupling parameters are obtained from drained and undrained experiments. It is convenient to express the strain and stress tensors of Equation 2 in terms of their volumetric and deviatoric parts

$$\boldsymbol{\varepsilon} = \frac{1}{3}\varepsilon_v \mathbf{1} + \mathbf{e}$$

Equation 7. Strain in terms of volumetric and deviatoric parts

$$\boldsymbol{\sigma} = \sigma_v \mathbf{1} + \boldsymbol{s}$$

Equation 8. Stress in terms of volumetric and deviatoric parts

where $\mathbf{e}$ is the deviatoric part of the strain tensor, σ_v is the volumetric (mean) total stress, ε_v is the volumetric strain, and $\boldsymbol{s}$ is the deviatoric total stress tensor.

Using the infinitesimal transformation, the governing equation of fluid flow is written as

$$\frac{\partial m}{\partial t} + \text{Div}\, \mathbf{w} = \rho_{f,0} f$$

Equation 9. Governing equation of fluid flow using infinitesimal transformation

where $\mathbf{w}$ is the fluid mass flux (fluid mass flow rate per unit area and time), $\rho_{f,0}$ is the fluid density, $\frac{\partial m}{\partial t}$ is the variation of the fluid mass relative to the solid skeleton, and f is the volumetric source term. Using the definition of Equation 4, we can write the above equation in terms of pressure and volumetric strain:

$$\frac{1}{M}\frac{\partial p}{\partial t} + b\frac{\partial \varepsilon_v}{\partial t} + \text{Div}\frac{\mathbf{w}}{\rho_{f,0}} = f$$

Equation 10. Coupled governing equation of fluid flow in terms of pressure and volumetric strain

The fluid velocity relative to the solid phase $\mathbf{v} = \frac{\mathbf{w}}{\rho_{f,0}}$ is given by Darcy's law:

$$\mathbf{v} = -\frac{\mathbf{k_p}}{\mu}\left(\text{Grad}\, p - \rho_f \mathbf{g}\right)$$

Equation 11. Fluid velocity relative to the solid phase

where $\mathbf{k_p}$ is the positive-definite absolute-permeability tensor, and μ is the fluid viscosity.

2.2 Coupling and Constitutive Relations Derivation

The coupling and constitutive relations were derived by adopting a classical continuum representation, where the fluid and solid are viewed as overlapping continua. In addition, the general coupling among mass, energy, and mechanical equilibrium were summarized based on the approach by Coussy (1995) and Coussy et al. (1998). For more information on the coupling derivation please refer to Kim (2010).

Assuming isothermal condition and isotropy, the constitutive relations of $\delta\sigma$, δp_J, and δS are reduced to the coupling between mass-flow and mechanics (Kim 2010)

$$\delta\sigma = \mathbf{C}_{ud} : \delta\varepsilon - \left(\frac{\delta m}{\rho}\right)_J M_{JK} b_K \mathbf{1}$$

Equation 12. Geomechanics coupling for multiphase flow

$$\delta p_J = M_{JK}\left(-b_K \delta\varepsilon_v + \left(\frac{\delta m}{\rho}\right)_K\right)$$

Equation 13. Flow coupling for multiphase flow

Equation 12 can be rewritten as

$$\delta\sigma = \mathbf{C}_{dr}\colon \delta\varepsilon - b_j \delta p_j \mathbf{1}$$

Equation 14. Geomechanics coupled equation in terms of drained bulk moduli

where $\mathbf{C}_{dr}$ represents the drained bulk moduli. In the case of single phase flow, Equation 13 and Equation 14 are further reduced to equations.

$$(\sigma_v - \sigma_v^0) = K_{dr}\varepsilon_v - b\left(p_f - p_f^0\right)$$

Equation 15. Geomechanics coupling for single phase flow

$$\frac{1}{\rho_{f,0}}(m - m_0) = b\varepsilon_v + \frac{1}{M}\left(p_f - p_f^0\right)$$

Equation 16. Flow coupling for single phase flow

2.3 Additional Equations

2.3.1 Modified Cubic Law

Since this thesis is concerned with planar fracture propagation, it is imperative to develop a mathematically appropriate permeability calculation. When material failure occurs, micro-fractures are created and connected, making macroscopic fractures. As a result, permeability can increase dramatically and discontinuously in time (Kim et al 2016). Because hydraulic fracturing creates fractures which significantly increase permeability by several orders, this thesis considers the change in permeability by using an explicit treatment modified cubic law.

Witherspoon et al. (1980) developed a modified cubic law validated by laboratory experiments on artificial tension fractures in samples of granite and marble. A general flow law is considered as

$$\frac{Q_f}{\Delta h} = \frac{C}{f_r}\left(b_f\right)^n$$

Equation 17. Witherspoon modified cubic law

where Q_f is the volume flow rate per unit plate (or fracture) width, Δh is head gradient, f_r is the friction factor that accounts for the roughness of the fracture surface, b_f is an apparent physical aperture, and C is a constant depending on the flow domain geometry and the properties of the fluid.

If $n = 3$, Equation 17 becomes a cubic law or modified cubic law, and in such case the apparent physical aperture b_f is related to the hydraulic aperture b_h as:

$$b_f = f_r^{\frac{1}{3}} b_h$$

Equation 18. Apparent physical aperture

Finally, making use of this definition, the fracture permeability is calculated as:

$$k_f = k_{f,0} \cdot \left(\frac{b_f}{b_h}\right)^3$$

Equation 19. Fracture permeability

where k_f is the permeability of the fracture, and $k_{f,0}$ is the inputted reference permeability of the fracture.

2.3.2 Fracturing Criteria

The tensile strength is employed as large-scale fracture propagation criteria. In general, the fracture toughness is utilized for investigating small-scale fracture propagation (Adachi et al 2007). According to Kim et al. (2013), the tensile failure can occur when

$$\sqrt{\frac{|\mathbf{t}_s|^2}{\beta^2}} + t_n^2 \geq T_c$$

Equation 20. Fracture criteria

where $\mathbf{t}_s$ and t_n are the shear and normal traction and T_c is the tensile strength of the material. β is a factor determining the contribution from both normal and shear effective stresses to the tensile failure. If $\beta \to \infty$, the tensile failure occurs purely due to normal traction, which is the assumption in this thesis. Assuming that the failure occurs when the difference between hydraulic fluid pressure in the fracture and in-situ normal stress in the rock exceeds the tensile strength of the rock, the simulator considers the gridblock as failed and calculates its new permeability using the modified cubic law (Equation 19).

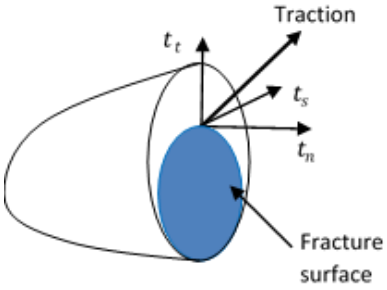

Figure 1. A schematic diagram for a planar fracture

2.3.3 Moment Tensor and MEQ's

Moment tensors provide a general theoretical framework to describe seismic sources based on generalized force couples. The moment tensor description is not restricted to earthquake sources, but covers also other types of seismic sources such as mixed mode ruptures driven by fluid and gas injections (Dahm and Kruger 2014).

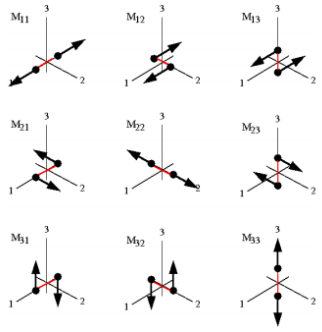

Figure 2. The system of force couples representing the components of a cartesian moment tensor. Reprinted from Dahm and Kruger, copyright 2014.

There are multiple sources of seismic waves in the Earth: earthquakes, explosions, tensile cracks, rock burst, or mass slope (Dahm and Kruger 2014). This study is restricted to those generated by regions under high fluid overpressure, which

correspond to hydraulic fracturing operations. These operations involve a source associated with a planar crack and a dislocation in an arbitrary direction as well as an opening of the rupture plane. The moment tensor of a general dislocation source was described by Aki and Richards (2002) as

$$M_{pq} = \int m_{pq} d\Sigma$$

Equation 21. Moment tensor of a general dislocation

where M_{pq} is defined as the seismic moment tensor, m_{pq} is the moment density tensor or dipole-moment density, Σ is the internal surface element (Figure 3), and the subscript pq refers to a particular couple combination.

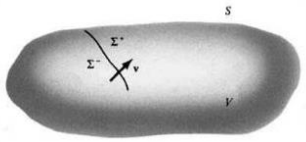

Figure 3. A finite elastic body, with volume V and external surface S, and an internal surface Σ. Reprinted from Aki and Richards, copyright 2002.

Furthermore, by assuming an isotropic medium and constant slip, the moment density tensor becomes

$$m_{pq} = \lambda v_k u_k \delta_{pq} + \mu(v_p u_q + v_q u_p)$$

Equation 22. Moment density tensor

where λ is Lame's first parameter, ^{v} is the internal surface normal vector, ^{u} is the displacement, δ_{pq} is the Kronecker symbol or delta, and μ is Lame's second parameter or shear modulus.

After calculating M_{pq}, it is customary to convert it to the seismic moment M_0. The seismic moment is a fundamental parameter used to measure the strength of earthquakes, which can range from about 10^{30} dyne-cm for big earthquakes to around 10^{12} dyne-cm for micro-earthquakes (Aki and Richards 2002). The seismic moment for a general dislocation source is obtained by L_2 norm (Equation 23) of the seismic moment tensor, as follows.

$$M_0 = \left|\left|\mathbf{M}\right|\right|_{L2}$$

Equation 23. Seismic moment

A special case of Equation 21 can be derived for the case of hydraulic fractures that involve purely shear forces. These micro-earthquakes generated are idealized by the physical model of a planar shear crack, which can be represented by two perpendicular force dipoles with zero angular momentum. Therefore, the shear crack source is often termed "double couple." The seismic moment for this special case (Dahm and Kruger 2014) is given by

$$M_0 = \sqrt{0.5 M_{pq} M_{pq}} = \mu A_f d$$

Equation 24. Seismic moment for purely shear forces

where A_f is the planar fracture area, and d is the mean (over the fractured area) of the amount of displacement (Kostrov 1974).

Kanamori (1977) introduced the concept of moment magnitude to seismology. This is simply a magnitude scale based on the seismic moment of an earthquake. The definition of the moment magnitude, denoted M_w, is

$$M_w = \frac{\log_{10} M_0 - 16.1}{1.5} + 4.667$$

Equation 25. Moment magnitude

The coupled flow and geomechanics simulator outputs the displacement of each of the grid nodes at every time step. Utilizing this information and combining it with the displacement derived form of Equation 22, the displacement outputs of the coupled flow geomechanics simulator and equations 23 and 25; it is possible to track MEQs location, magnitude and timing. Where c_{pqrs} is the stiffness tensor and Δu_{rs} is the nodal displacement change.

$$M_{pq} = \int c_{pqrs} \Delta u_{rs} d\Gamma$$

Equation 26. Moment density tensor in terms of displacement

3. NUMERICAL MODELLING

3.1 Discretization

For time discretization, this thesis adopted the backward Euler method, which is widely used in reservoir simulation. In space discretization, the finite element method is used for geomechanics while the finite volume method is used for fluid (Kim et al 2011). These particular space discretizations are practical because the finite volume method is employed in most reservoir simulators and the finite element method is widely used in geotechnical engineering, so the mix-space discretizations allow for the use of robust flow and geomechanics simulators. Also, these mix-space discretizations can provide advantages such as local mass conservation and better numerical stability in space when compared with discretizations using finite element method for both flow and geomechanics. Additionally, the mix-space discretization choice is practical for solving the primary unknows and follows an intuitive order when making use of reservoir and geomechanical simulators in a sequential fashion (Kim 2010).

3.2 Failure Modelling

For failure modelling, this thesis refers to the process developed by Kim and Moridis (2013). Failure is modeled by introducing new internal Neumann boundaries by splitting nodes when fracturing occurs, and assign the traction from the fluid pressure inside the fractures. The node splitting is performed based on the tensile failure condition, as described in section 2.3.2. This thesis focuses on vertical tensile fracturing,

which is reduced from a general planar fracture due to no horizontal displacement condition at the plane that contains the vertical fracture due to symmetry. A schematics of the fracture plane is shown on Figure 4, which shows its location at the outside boundary.

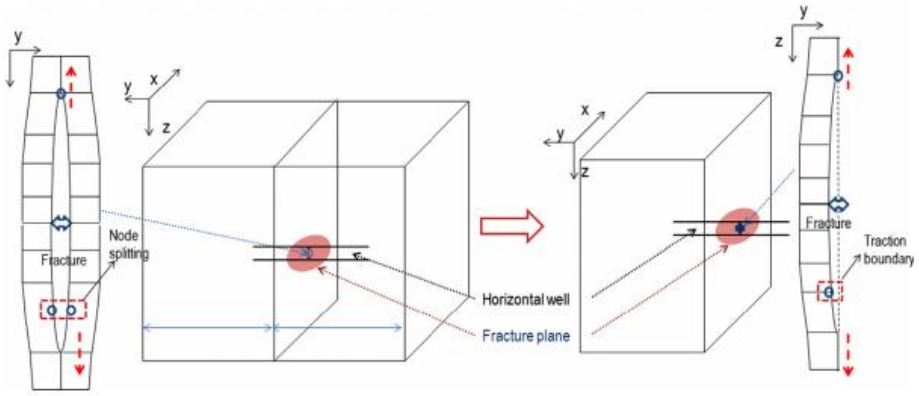

Figure 4. Schematics of hydraulic fracturing in 3D. General type of planar fracturing (left) and vertical propagation of a fracture (right). Reprinted from Kim and Moridis, copyright 2013.

3.3 Solution Scheme

In this study, the simulator employed the modified fixed stress sequential implicit method to solve coupled flow and geomechanics, which provides unconditional numerical stability and high accuracy (Kim et al. 2011). Using the fixed stress split, the flow problem is solved first by fixing the total stress field, where the strain and displacement fields are allowed to change. Then, the geomechanics problem is solved on the basis of the solutions obtained from the previous flow problem, such as fluid pressure, saturation, and temperature. This sequential method can easily be implemented

by the Lagrange porosity function Φ and its correction term $\Delta\Phi$, written as a form of the staggered approach as,

$$\Phi^{n+1} - \Phi^n = \underbrace{\left(\frac{b^2}{K_{dr}} + \frac{b - \Phi^n}{K_s}\right)}_{\Phi^n c_p}\left(p_f^{n+1} - p_f^n\right) + \underbrace{\frac{b}{K_{dr}}\left(\sigma_v^n - \sigma_v^{n-1}\right)}_{\Delta\Phi}$$

Equation 27. Lagrange porosity correction for homogeneous isothermal single phase.

Where c_p is the pore compressibility in conventional reservoir simulation (Aziz and Settari 1979), and σ_v is the total (volumetric) mean stress, Φ is defined as the ratio of the pore volume in the deformed configuration to the bulk volume in the reference (initial) configuration. The porosity correction term ΔΦ, is calculated from geomechanics, which corrects the inconsistency between the porosity estimated from the pore compressibility of the uncoupled flow problem and the strain from geomechanics. The fixed-stress sequential method solves two-way coupling between flow and geomechanics. This method is able to capture the Mandel-Cryer effects, solving Mandel's problem correctly, which cannot be solved by uncoupled simulation. This form of sequential solution follows the algorithms proposed by Wang et al. (2004).

3.4 Simulators

This thesis employs a sequentially coupled flow and geomechanics simulator. The coupled sequential solution strategy allows the use of existing robust flow and geomechanics simulators by constructing an interface between them (Settari and Mourits

1998). This thesis uses TOUGH+ as a fluid and heat flow simulator and ROCMECH for a geomechanics simulator, namely T+M, and developed in the Lawrence Berkeley National Laboratory (Kim and Moridis 2013). It is important to note that although geomechanics is simulated in 3D, only flow through the hydraulic fracture is considered. As a result, the domain of geomechanics is larger than that of flow. Additionally, there are no-horizontal-displacement boundary conditions for the sides, except for the fracture nodes, with no displacement boundary at the bottom. Furthermore, there is additional traction on the top of the domain.

3.5 Bend Arch-Fort Worth Basin Domain Generation

This thesis investigates horizontal and vertical well hydraulic fracturing in the Barnett shale located in the Bend Arch-Fort Worth Basin.

3.5.1 Mechanical Properties

Using a wire-line-log study and resistivity logs of the Bend Arch-Forth Worth Basin (Perez and Marfurt 2013), and combining it with geomechanical studies conducted in the Barnett Shale (Almon et al 2005; Bhandari et al 2015; Eshkalak et al 2014; Fisher et al 2002; Marinos et al 2000; Hargrove et al 2015; Pollastro et al 2003; Vermylen and Zoback 2011), it was possible to determine the thickness and geomechanical properties of the productive important layers of the Bend Arch-Fort basin (Fig. 8): Lower Marble Falls, Upper Barnett, Forestburg, Lower Barnett, Viola/Simpson formations.

Using this information, a structured grid was created with different layer properties to simulate flow and geomechanical coupling of a real reservoir problem. Because the reservoir is highly heterogeneous and anisotropic, its properties vary greatly depending on direction. This thesis assumed homogeneous horizontal properties are equal but not vertically. Other used material properties are presented on Table 1.

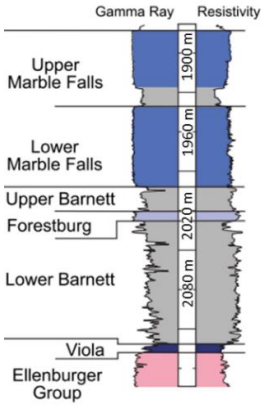

Figure 5. Wire-line-log of Bend Arch-Fort Worth Basin. Reprinted from Loucks and Ruppel, copyright 2007.

In addition of modelling five layers with different characteristics, the well cement layer was also model using mechanical properties obtained from C. Solutions MMS Project. The wellbore cement casing properties corresponding to the last column of Table 1.

Property (units)	Formation					Well Cement
	Lower Marble Falls	Upper Barnett Shale	Forestburgh Limestone	Lower Barnett Shale	Viola/Simpson	
Porosity	4%	5%	5%	5%	4%	-
Poisson's Ratio	0.27-0.34	0.2	0.3	0.2	0.31	0.2
Young's Modulus (Gpa)	75.00	45.00	65.00	48.00	70.00	6.27
Shear Modulus (Gpa)	28.85	18.75	25.00	20.00	26.72	2.61
Biot's coefficient	0.89	0.86	0.91	0.85	0.90	0.80
Tensile Strength (MPa)	30.00	10.00	25.00	13.00	28.00	1.47
Bulk Density (kg/m3)	2710.00	2490.00	2700.00	2500.00	2720.00	1797.40

Table 1. Formations main mechanical properties

3.5.2 Stress Field

After defining the mechanical properties the next step was to generate a representative stress field for the reservoir. Zoback et. Al (2014) mapped the principal stress across the US (Figure 6).

From the map and superposing the Barnett shale location, it is possible to conclude that the reservoir is located in a "pure normal faulting" environment. This has significant ramifications into fracture modelling as normal faulting environment constraints the magnitudes of the principal stresses. Under pure normal faulting, the magnitude of the vertical stress (S_V) is greater than the maximum horizontal stress (S_{Hmax}) which in turn is larger than the minimum principal horizontal stress (S_{hmin}).

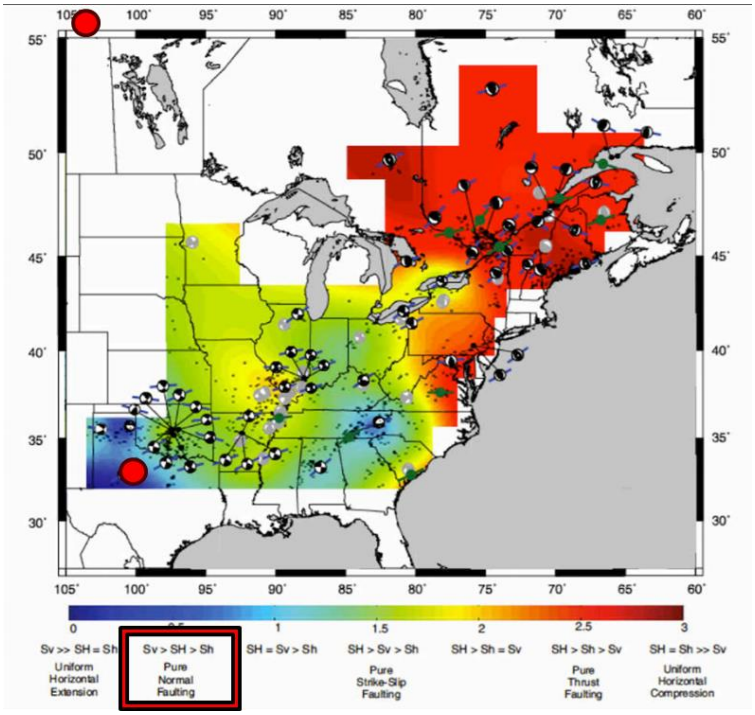

Figure 6. Principal stresses across the United States. Reprinted from Zoback et al , copyright 2014.

Vermylen (2011) used a density log to obtain a range of vertical stress values of the formation, also analyzing FMI logs for both vertical and horizontal sections of a pilot well to map natural fractures and record wellbore failures. This can accurately constraint the vertical, minimum and maximum horizontal stresses, shown in Table 2.

Stress Orientation	Value (Pa/m)	Top Grid Stresses (MPa)
Vertical Stress ($\|S_V\|$)	25000	45
Minimum Horizontal Stress ($\|S_h\|$)	14,250-15,400	28
Maximum Horizontal Stress ($\|S_H\|$)	20,000 ≤	36
Pore Pressure	11310	18.0

Table 2. Stress regime and reservoir pore pressure

For numerical simulation purposes, the top grid stresses were calculated by following a linear stress distribution path from the slopes defined by Vermylen. Pore pressure was assumed to be hydrostatic (~11,000 Pa/m) throughout the reservoir.

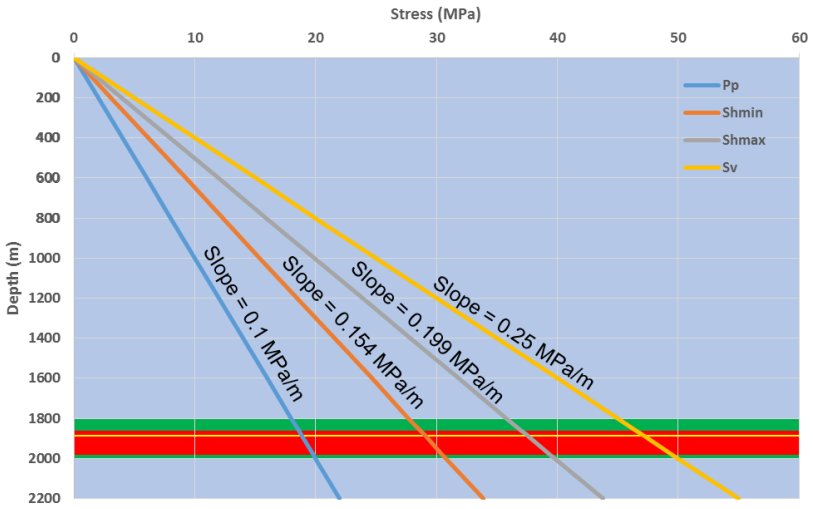

Figure 7. Reservoir stress and pressure field distribution.

As a result, the vertical stress equals 45.0 MPa, the maximum horizontal stress equals 35.82 MPa, the minimum horizontal stress equals 27.72 MPa and the pore pressure equals 18.0 MPa at the top of the reservoir domain (1800 meters of depth).

3.5.3 Grid Generation

The generated mesh used in the numerical simulations corresponds to a 50x3x57 grid system. The **x** direction has a grid spacing of 3 meters everywhere except close to the wellbore (25th and 26th gridblocks), where it refines to 0.3 meters for stability purposes. The **z** direction has a 3 meters uniform grid spacing for the Upper and Lower Barnett shale layers, as well as the Forestburg, but it has a spacing of 5 meters for the other layers (Lower Marble Falls and Viola/Simpson). Finally, spacing in the **y** direction increases subsequently and corresponds to 0.01, 2, 40 meters respectively.

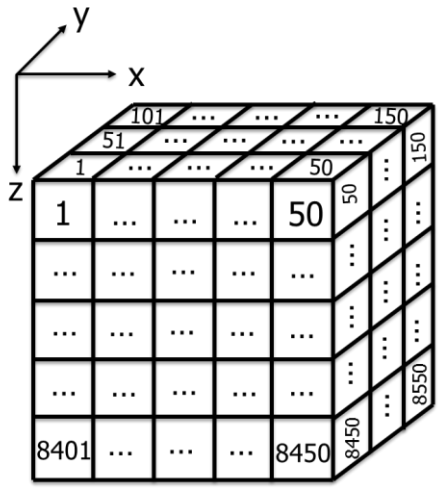

Figure 8. 3D mesh numbering of the simulation domain

4. NUMERICAL EXAMPLES

This chapter covers the numerical results of modelling planar fracture propagation and MEQs during hydraulic fracturing stimulation of the Barnett shale. It is divided into vertical and horizontal well simulation, as well as includes a sensitivity analysis of the simulator inputs for the horizontal well case.

4.1 Vertical Wells

4.1.1 Original Stress Field

The first simulation case corresponds to a domain with initial fracture nodes shown on Figure 10 with a stress field corresponding to Figure 9. The stress field shown on Figure 9 is simply a zoomed-in version of Figure 7.

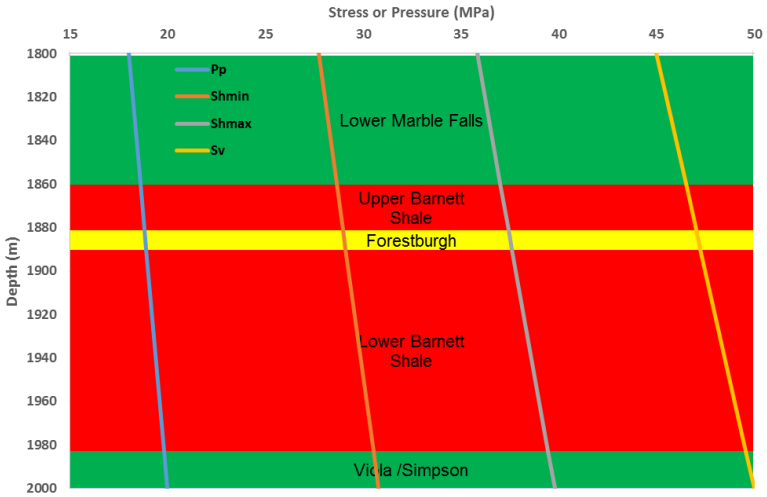

Figure 9. Stress field for first case

Furthermore, the simulated water injection occurred on vertical 28th to 35th nodes depicted below Figure 10. It is important to note that water was injected solely into the Bottom Barnett, and the injection points overlap the initial fracture blocks. The injection rate was taken to be 100 bbl/min for this simulation. Plots of this section correspond only up to 20 minutes because the majority of the fracturing occurs at early times.

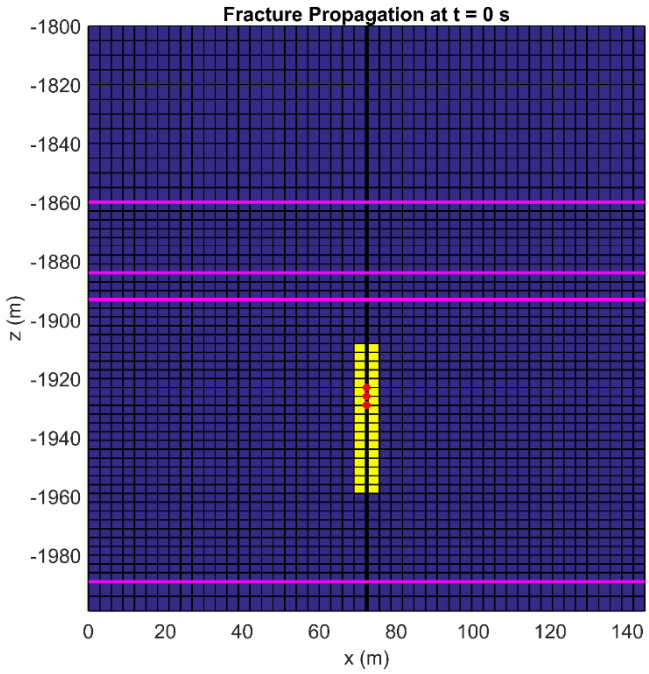

Figure 10. Initially fractured areas for a vertical well. Yellow blocks symbolize fractured grids. Magenta lines corresponds to transitions between layers. Red dots correspond to injection points

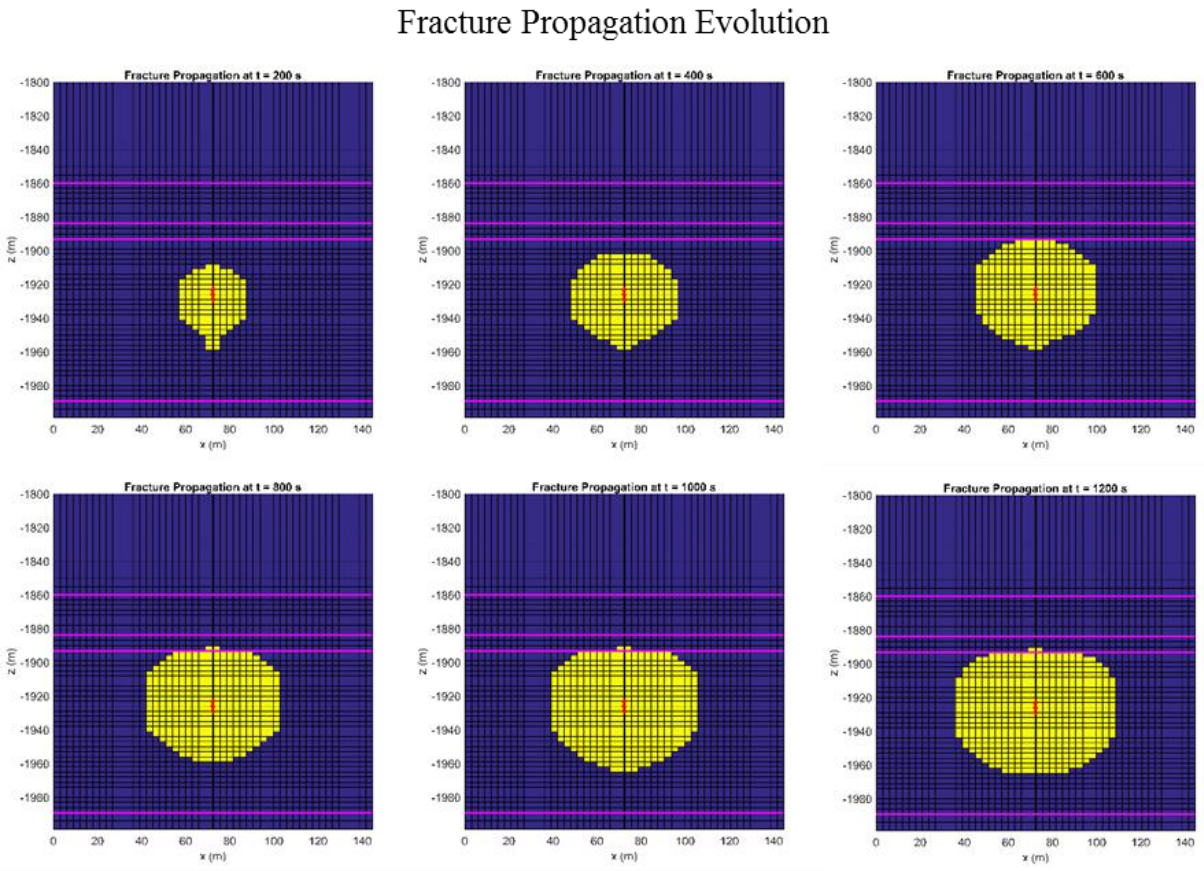

Figure 11. Fracture propagation every 200 seconds. Yellow blocks symbolize fracture nodes within a gridblock, while blue blocks represent intact rock gridblock. Magenta lines corresponds to transitions between layers. Red dots correspond to injection points

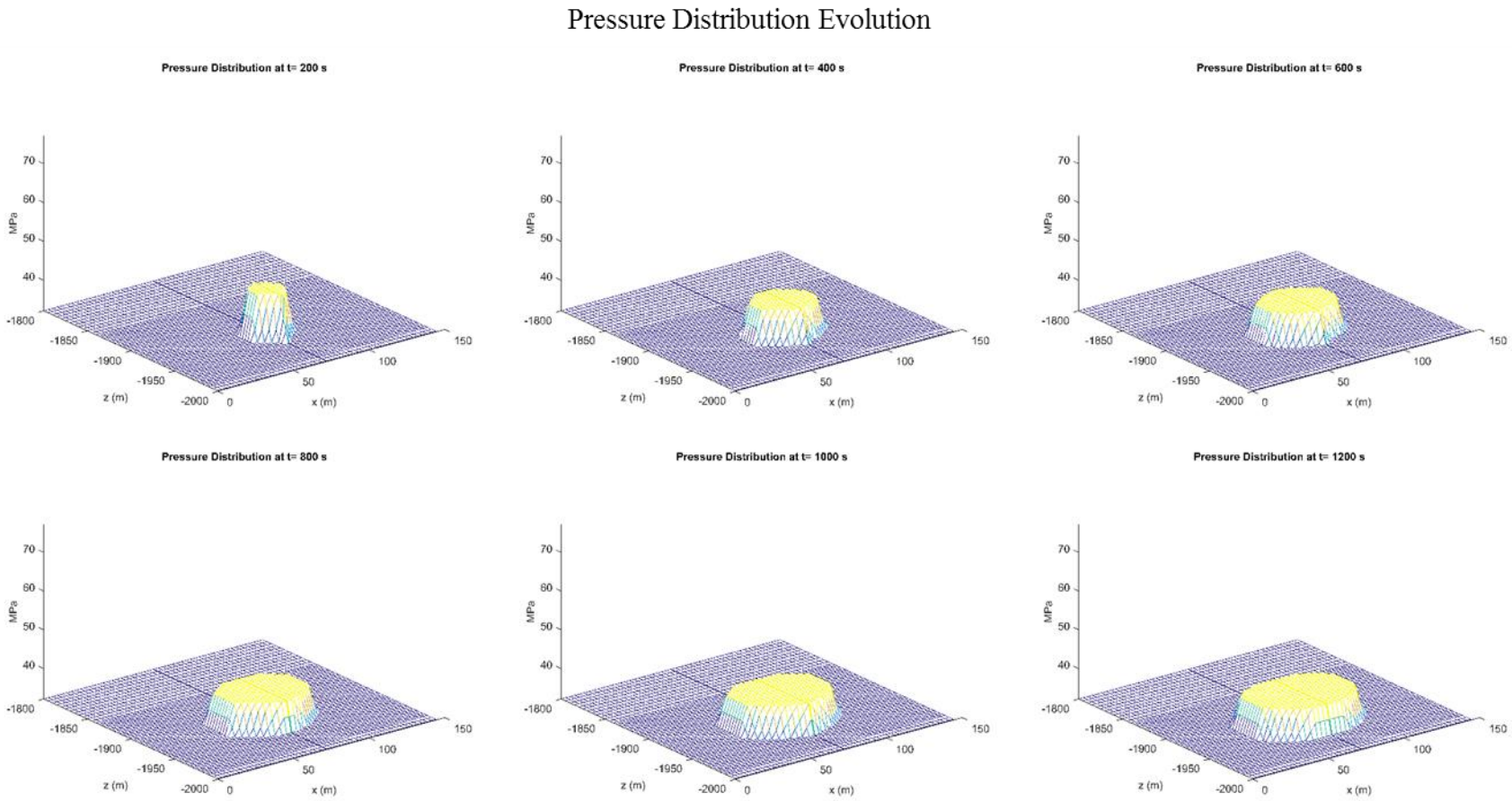

Figure 12. Pressure distribution every 200 seconds.

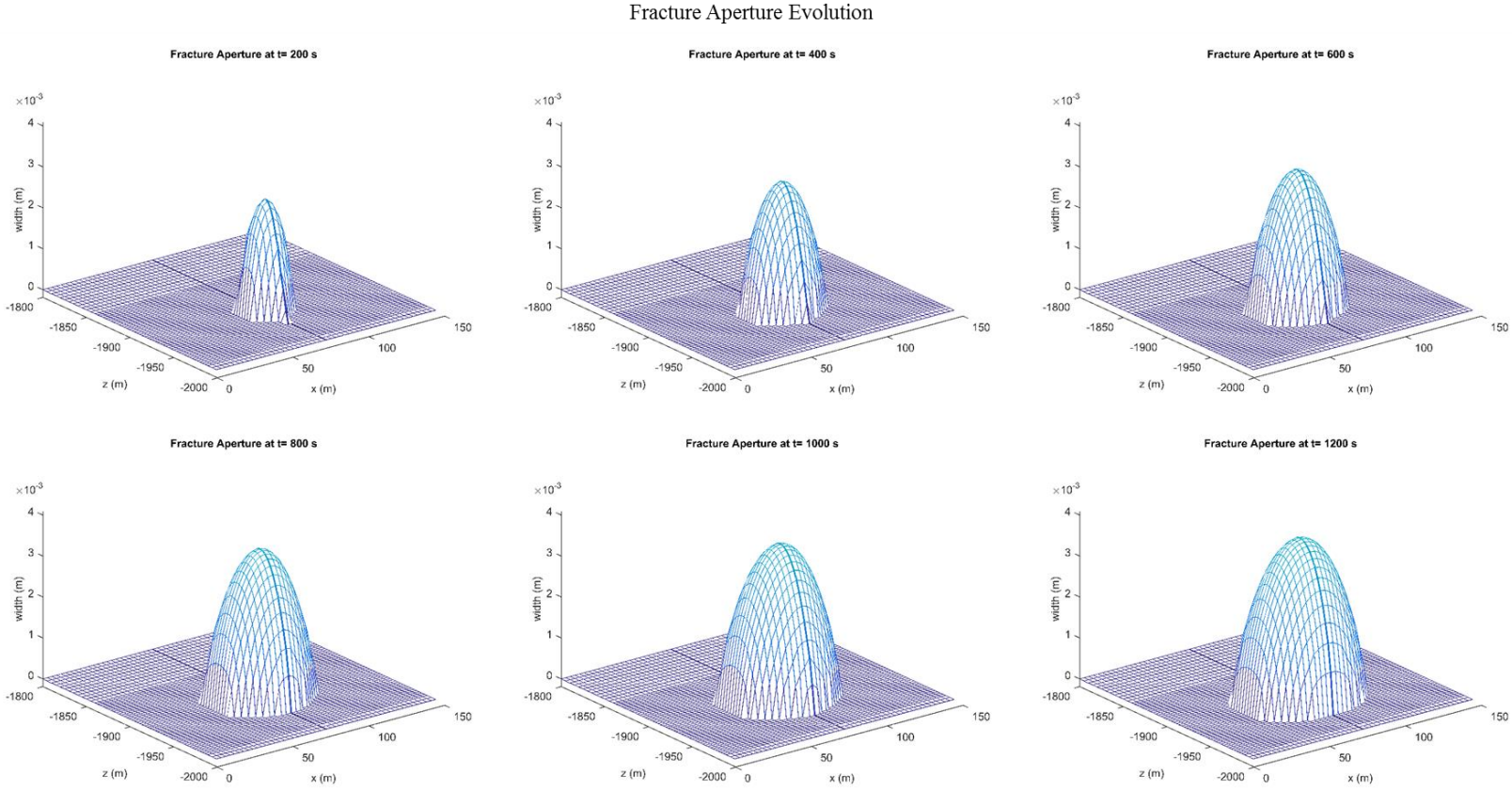

Figure 13. Fracture opening evolution every 200 seconds.

The fracture propagation is depicted below in a series of plots at different simulation times, shown in Figure 11. The fracture mainly propagates within the Lower Barnett area, not penetrating into Forestburg, because the tensile strength of Forestburg is higher than that of Lower Barnett.

Figure 12 shows that the pressure distribution stays below 50 MPa, and decreases in magnitude and increases in area as more water is injected. This is a result of the fracture gridblocks. As the pressure from water injection is divided among more fracture gridblocks, the pressure intensity decreases. This sharp contrast in pressure and area explains why the fracture propagation slows down as time goes on.

Figure 13 shows that the half fracture opening is mostly below 4 mm, with the maximum fracture opening occurring at later injection times. These openings translate into high permeability. The enhanced permeability delivers geomechanical loading from fluid injection to the areas away from the well. Also, the highest fracture openings occur at the injection points because of the increase pressure this area has when compared to the surrounding grids.

Unlike the pressure distribution, fracture aperture increases as injection time increases. On the first snapshot (when the injection time is 200 seconds) the fracture aperture reaches 3mm in contrast to the 4 mm of aperture at the latest snapshot (when the injection time is 1200 seconds). Additionally, as the fracture grows the constant injection keeps increasing the fracture aperture. The highest aperture corresponds to the injection points as pressure is the highest at those gridblocks.

Figure 14 shows the total number of nodes fractured over the total simulation time, from which the propagation stability can be identified.

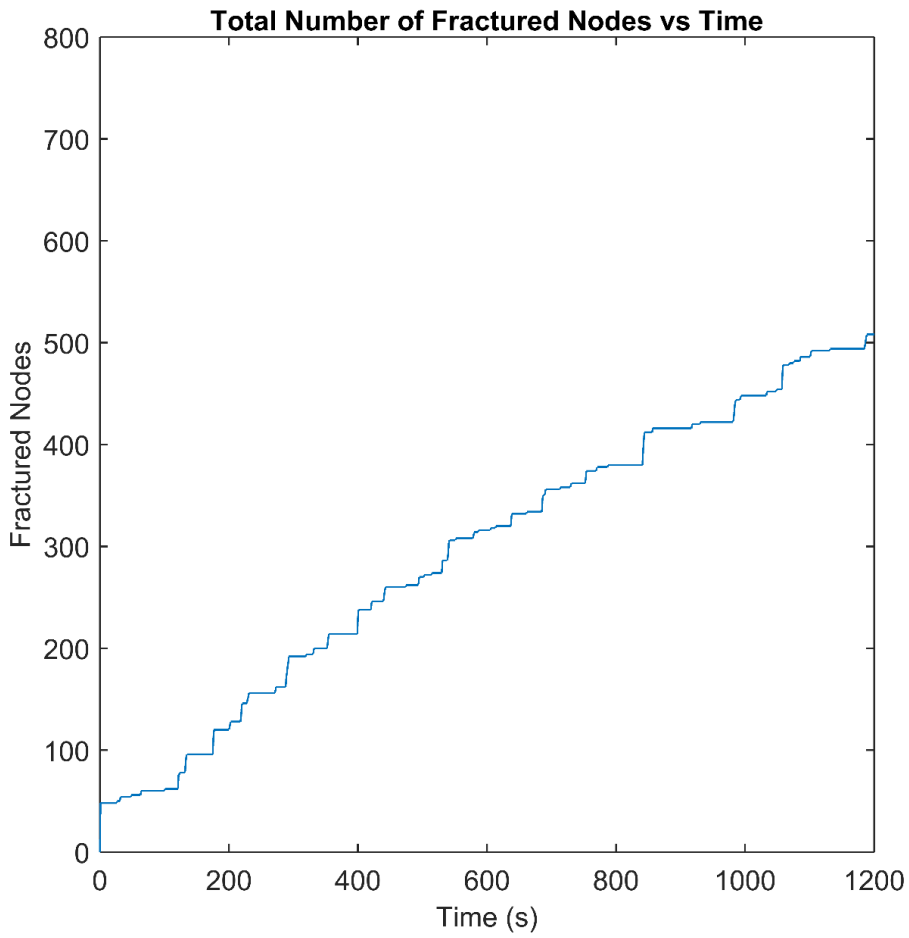

Figure 14. Total number of fracture nodes over time.

The results of the modelling for micro-seismicity are shown in Figures 15-18, based on geomechanics solution, such as displacements and areas of fractured nodes. These MEQ events are tracked through time as the fracture propagation occurs and by

specific location in the x-z plane to obtain a clear picture of how they relate to planar fracture propagation (i.e., 4 dimensional data).

From Figure 15, the moment magnitude (M_w) is, for the most part close to zero, which is well below safety concerns but it can still be recorded by a seismographer. From Figs 26-28 that the MEQ locations correspond to the fracture propagation. This implies that, given measured MEQ data, the forward coupled flow-geomechanics-MEQ geophysics simulation can be used to characterize reservoir properties through history matching. Rock properties like elastic moduli, tensile strength, initial distributions of total stress and pore-pressure can be back calculated.

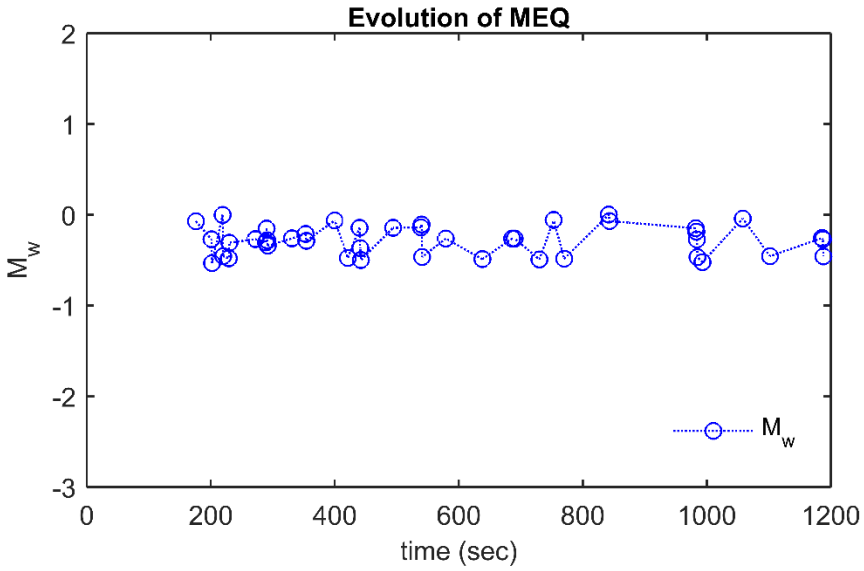

Figure 15. Evolution of moment magnitude (M_w) over time.

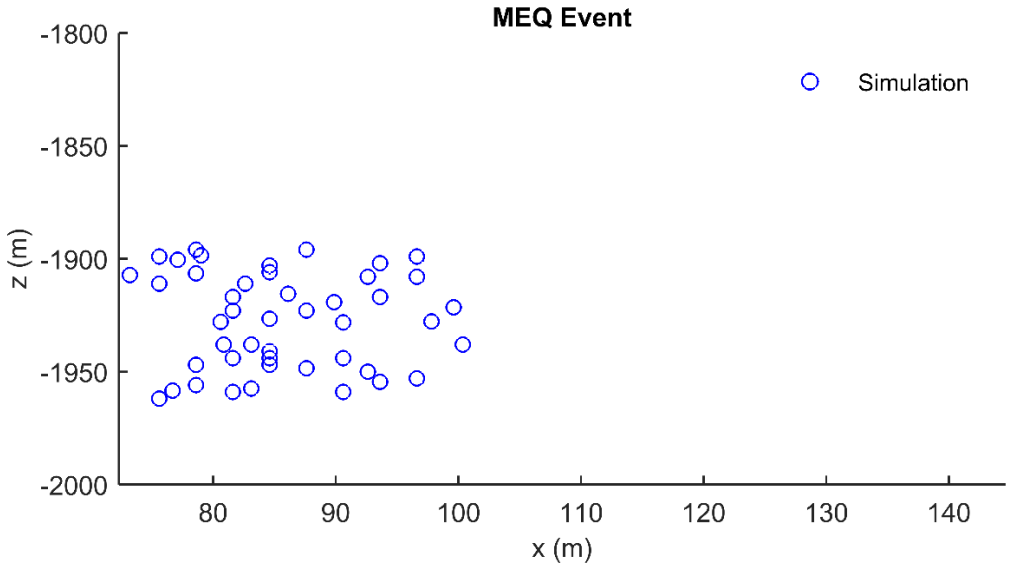

Figure 16. x-z location of MEQ's events (the right side of the fracture plane).

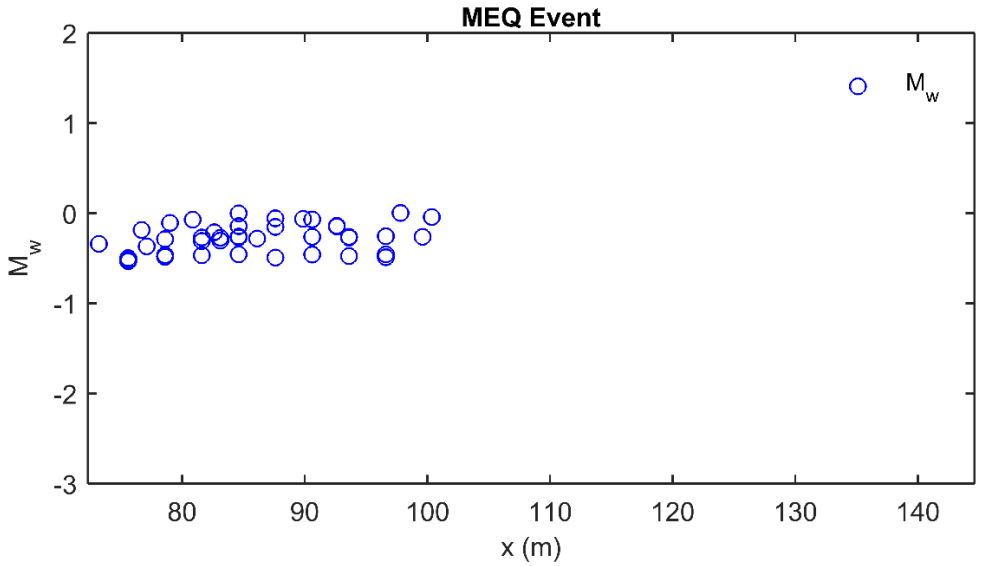

Figure 17. Location and moment magnitude (M_w) of MEQ's on x-direction (the right side of the fracture plane).

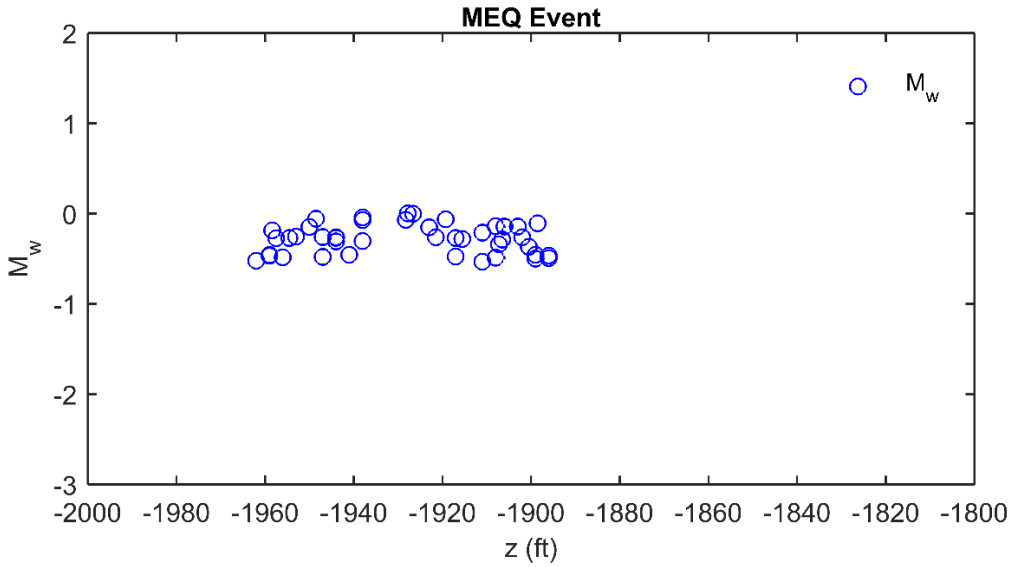

Figure 18. Location and moment magnitude (M_w) of MEQ's on z-direction.

From Figure 17 the MEQ locations are clustered nearby the wellbore. Additionally, from Figure 18 it can be observed that the MEQ even location is bound between the Forestburgh and Viola/Simpson formation.

Average	-0.2812
Range	0.0015 to -0.5322

Table 3. MEQ result summary for Lower Barnett simulation

4.1.2 Perturbation of the Stress Field Case

This thesis investigated under what conditions a fracture would migrate upwards and propagate on a different layer. This has potential harmful ramifications as a "run-away" fracture could potentially contaminate a nearby aquifer. It is known within petroleum engineering that fracture propagation hardly ever follows the design criteria: target lengths are not reached, proppant penetration is not satisfactory, and in some

instances fractures occur at a different depth than that of the injection point. Making use of the coupled simulator, this thesis conducted a physically rigorously study to find out under which conditions undesired fractures may occur.

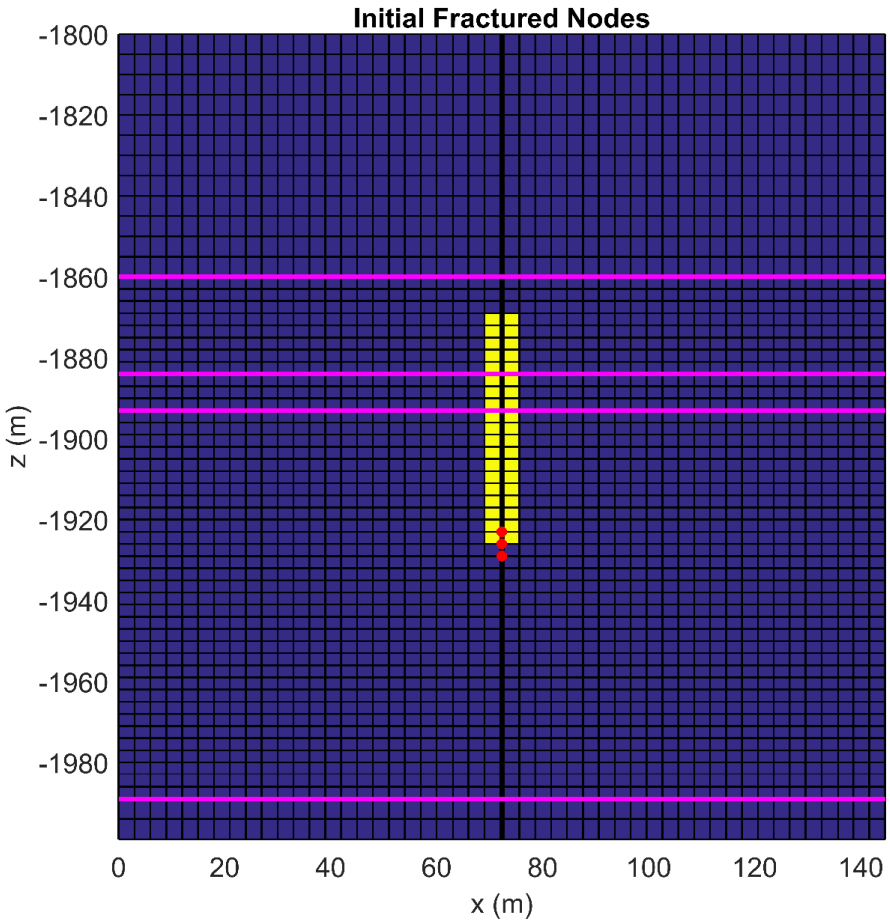

Figure 19. Initially fractured areas for a vertical well. Yellow blocks symbolize fractured grids. Magenta lines correspond to transitions between layers. Red dots correspond to injection points

To this purpose, this simulation used the same domain discretization and the same rock properties as the previous section. The main difference between the two

simulation cases is that the *Original Stress Field (Section 4.1.1)* case assumes additional nodes along the cement casing to be initially fractured (Figure 19). The assumption of fractured nodes between the Bottom and the Upper Barnett shale can be justified through well stability shear failure of the binding between steel casing and cement due to poor cementing (Kim et al 2016). Additionally, this case perturbed the horizontal stresses when compared to the first case (Figure 20) in order to encourage upward fracture migration. Moreover, the water was injected on the same nodes as the previous case.

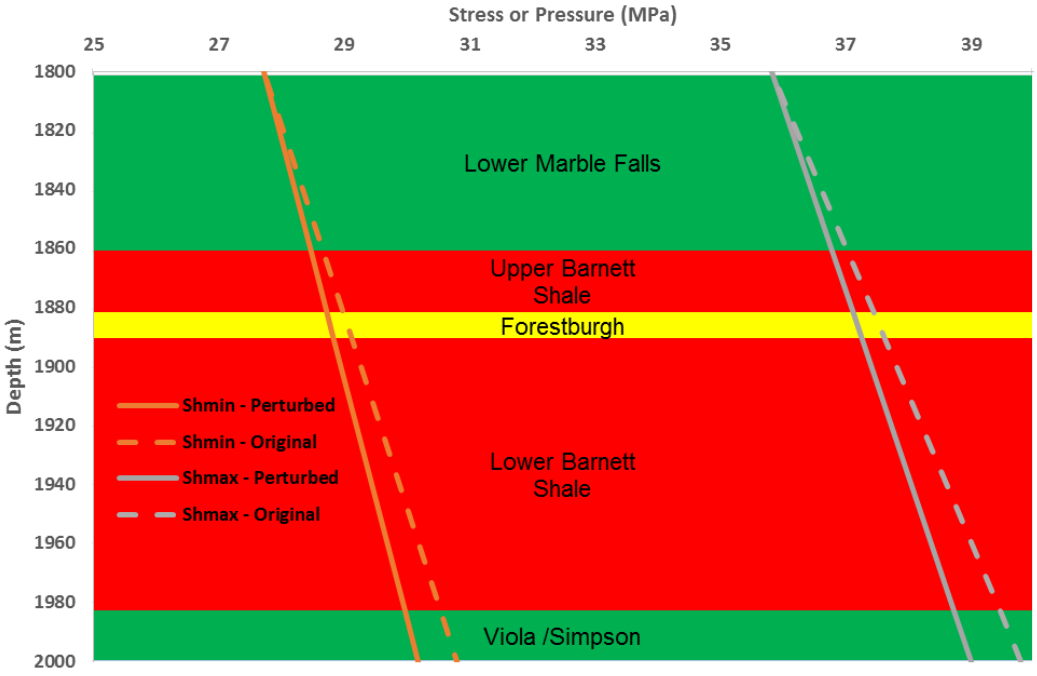

Figure 20. Perturbed stress field for second simulation case.

The fracture propagation is depicted below in a series of plots at different simulation times, shown in Figure 20. The fracture only propagates within the Upper

Barnett shale despite water being injected into the lower layer. Furthermore, the fracture did not penetrate into Forestburg because its tensile strength is much higher than that of either shale layer. Additionally, the fracture was confined entirely between the Lower Marble Falls and the Forestburg layers. Both the Lower Marble Falls and the Forestburg are composed mostly of limestone which has a higher tensile strength than shale. The Lower Marble Falls and Viola/Simpson formation have been regarded as “frac barriers” by the industry because of their ability to stop fractures from vertically propagating any further.

Figure 21 shows that the pressure distribution stays below 45 MPa, which is slightly lower than on the previous section.

Figure 22 shows that the half fracture opening is mostly below 3 mm, with the maximum fracture opening occurring at later injection times. The fracture aperture at the Upper Barnett is slightly narrower than on the Lower Barnett.

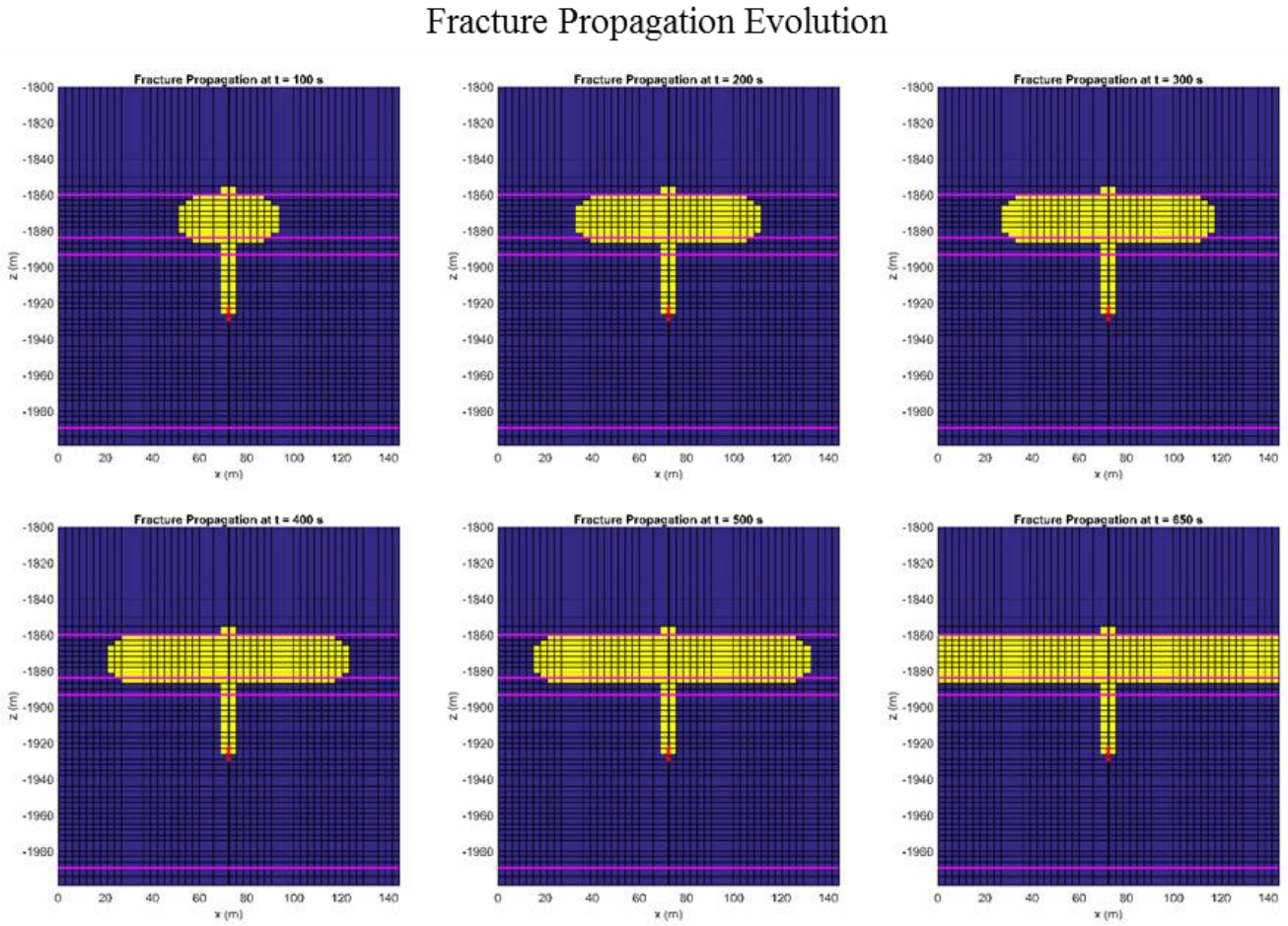

Figure 21. Fracture propagation at different times. Yellow blocks symbolize fracture nodes within a gridblock, while blue blocks represent intact rock gridblock.

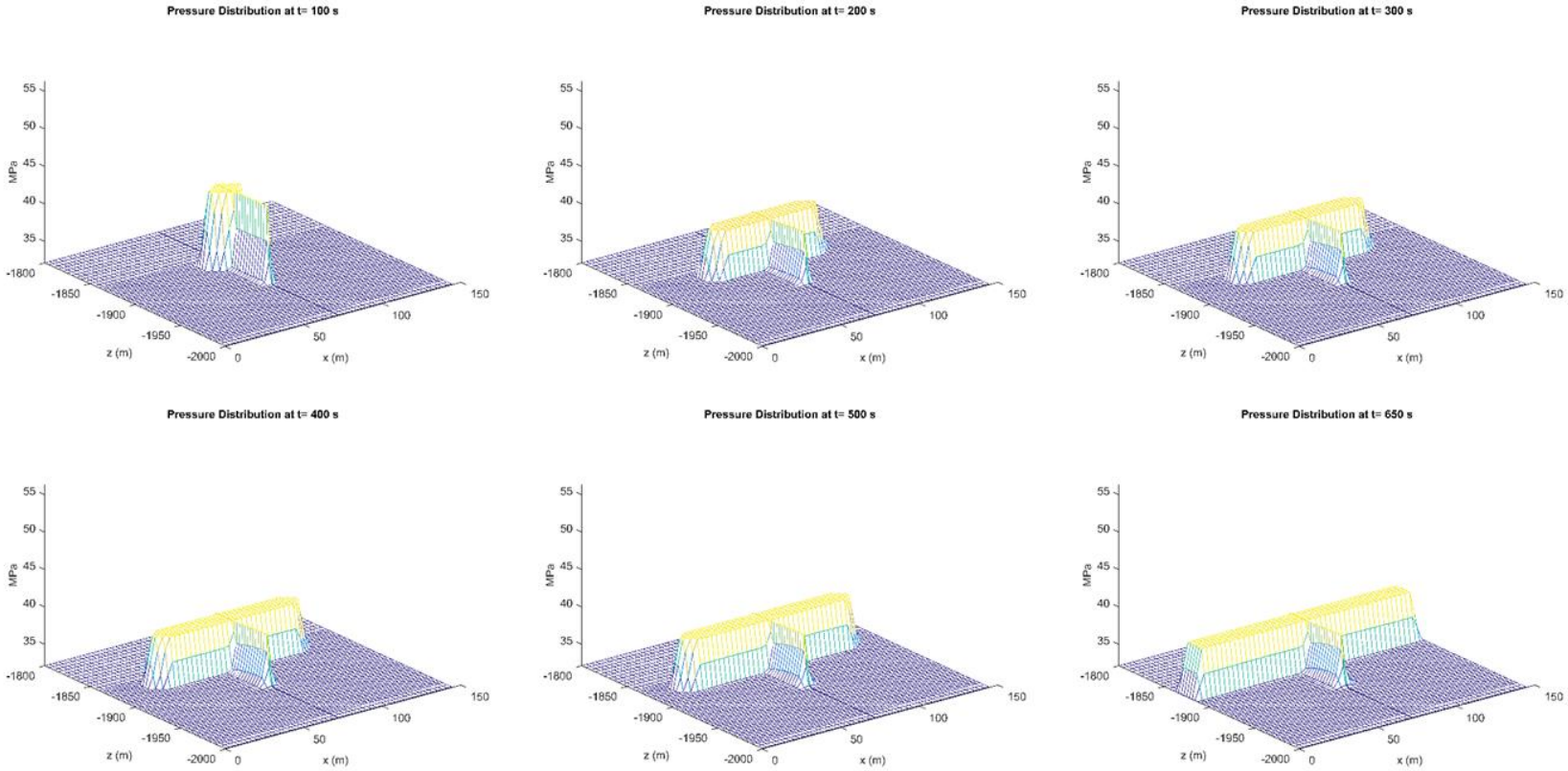

Figure 22. Pressure distribution evolution mesh.

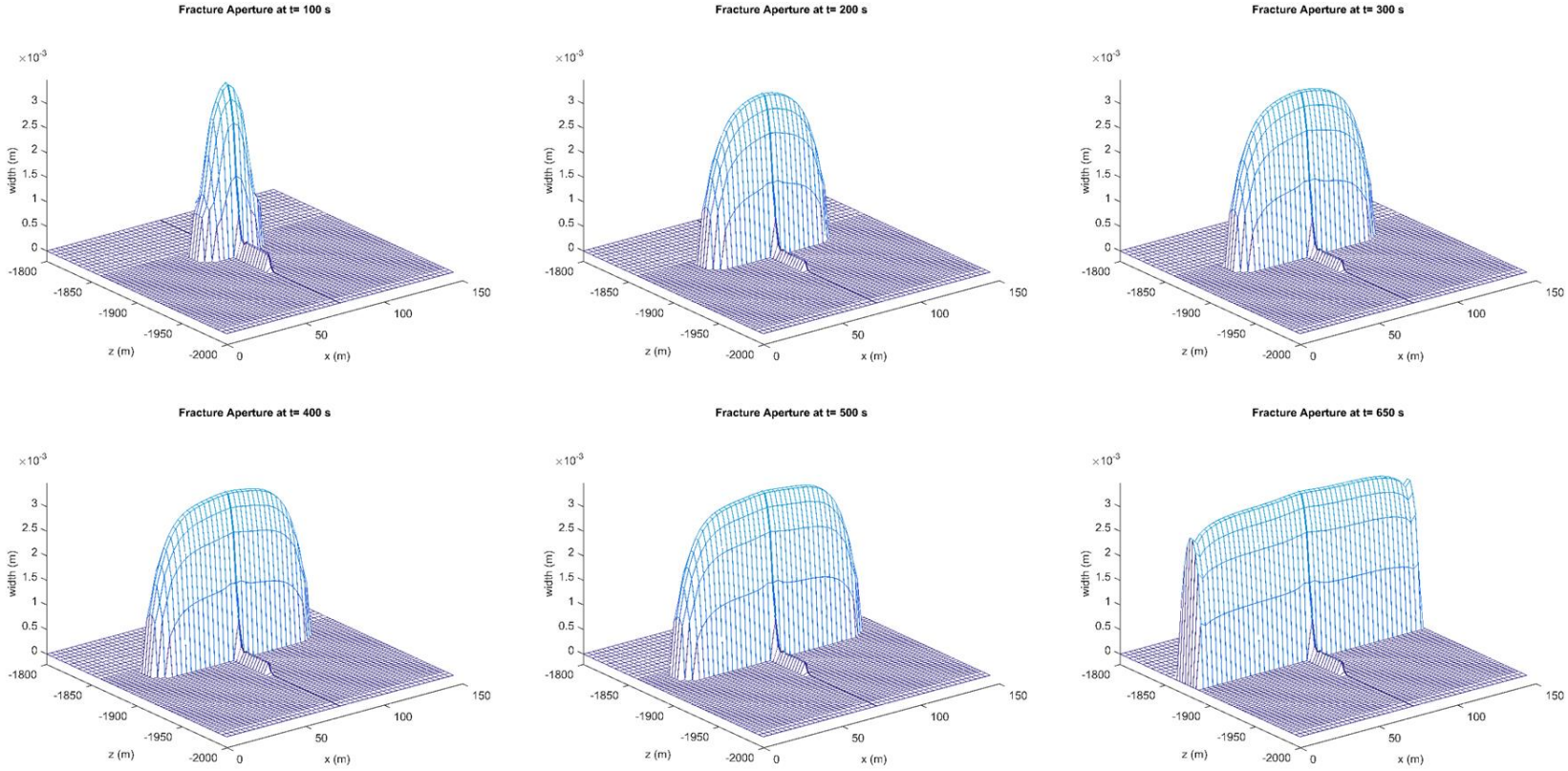

Figure 23. Fracture opening evolution mesh.

Figure 24 shows the total number of nodes fractured over the total simulation time, from which the propagation stability can be identified. Unlike the previous simulation, which had a stable fracture propagation, the Upper Barnett example is characterized by a jump at initial times, which translates into rapid initial fracture propagation.

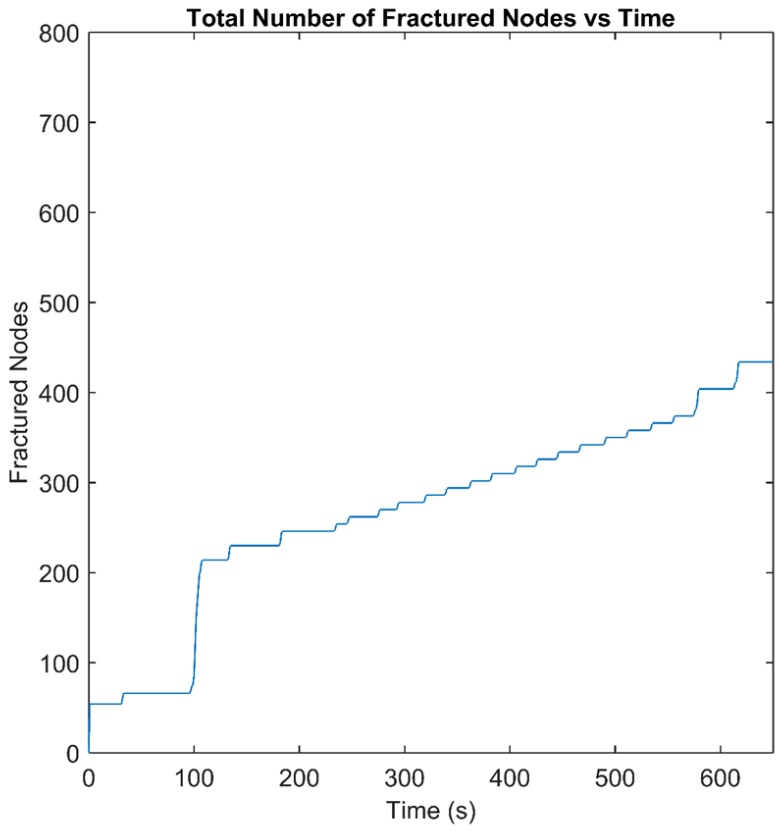

Figure 24. Total number of fracture nodes over time.

The MEQ simulation results for this section are shown in Figures 25-28**.** From Figure 25 M_w is again mostly around 0. We can identify from Figures 26- 28 that the

MEQ locations correspond to the fracture propagation. This further reinforces the possibility of history matching reservoir properties using measured MEQ data and a forward coupled flow-geomechanics-MEQ geophysics simulator.

Average	-0.0146
Range	0.5540 to -0.0146

Table 4. MEQ result summary for Upper Barnett simulation

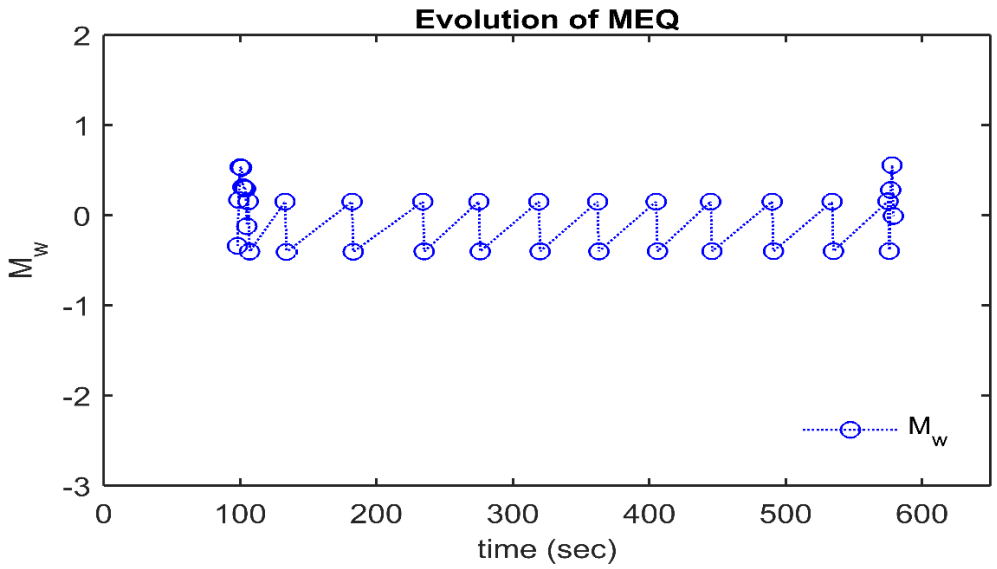

Figure 25. Evolution of moment magnitude (M_w) over time.

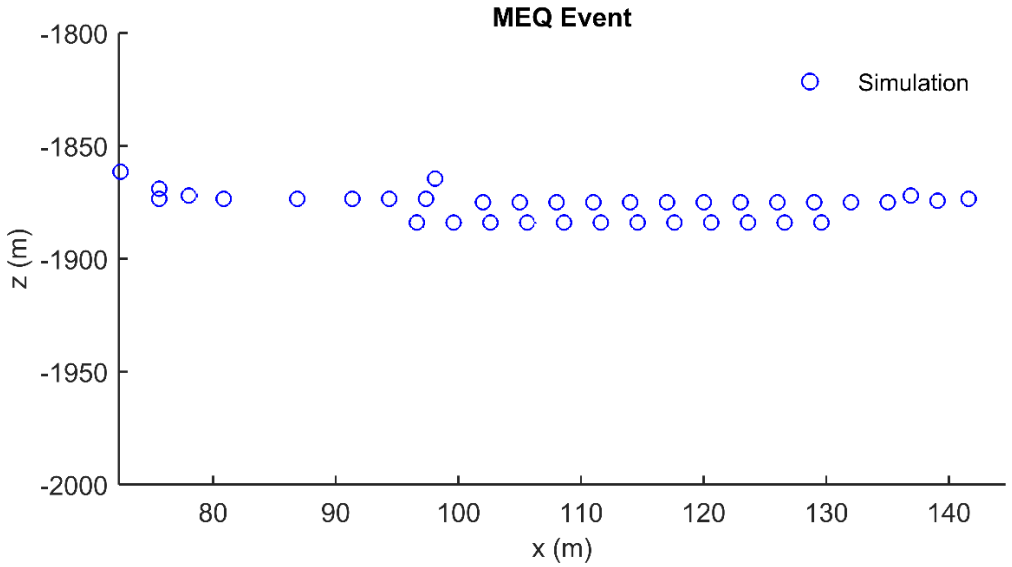

Figure 26. x-z location of MEQ's events (the right side of the fracture plane).

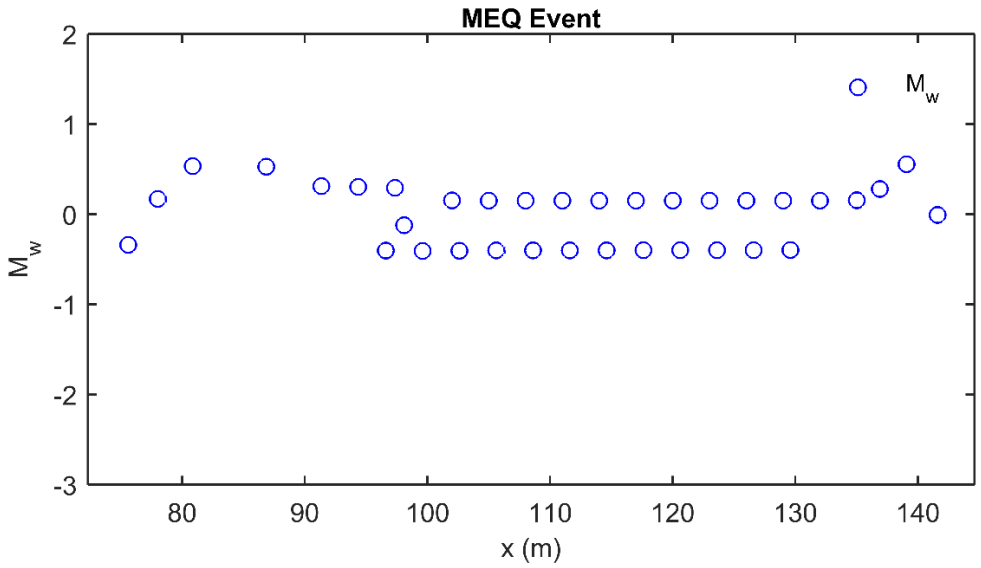

Figure 27. Location and moment magnitude (M_w) of MEQ's on x-direction (the right side of the fracture plane).

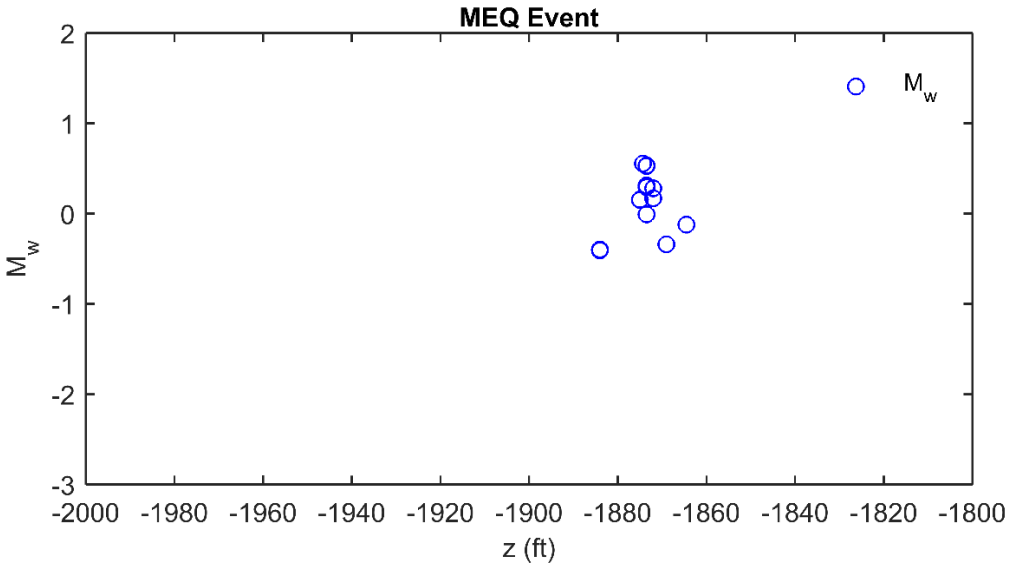

Figure 28. Location and moment magnitude (M_w) of MEQ's on z-

4.2 Horizontal Wells

4.2.1 Horizontal Fracturing Simulation

In addition to simulating vertically stimulated wells, this thesis also studied the effects of fracture propagation in horizontal wells. Assuming several horizontal wells with simultaneous fracturing at different locations, the simulation domain can be simplified by symmetry, shown in Figure 29.

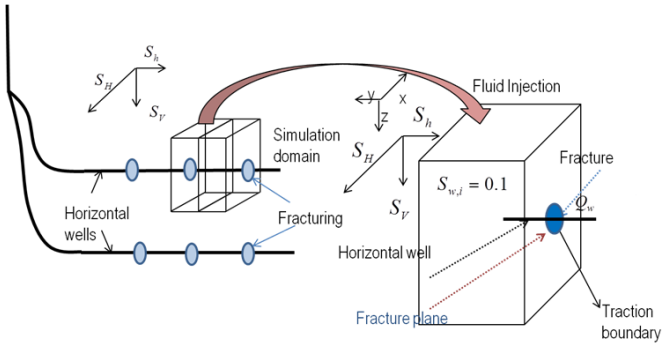

Figure 29.Schematics of hydraulic fracturing simulation with horizontal wells. Reprinted from Martinez et al, copyright 2016.

The discretization, mesh generation and initial conditions of the reservoir domain remain the same as for the vertical wells. The only difference comes from the initial fracture node distribution and injection rate. The injection rate was lowered to 90 bbl/min treatment to account for frictional loses away from the heel of the well. With water injected, the hydraulic fracture propagates further horizontally because the bounding layers have higher tensile strength and higher magnitude of minimum horizontal stress.

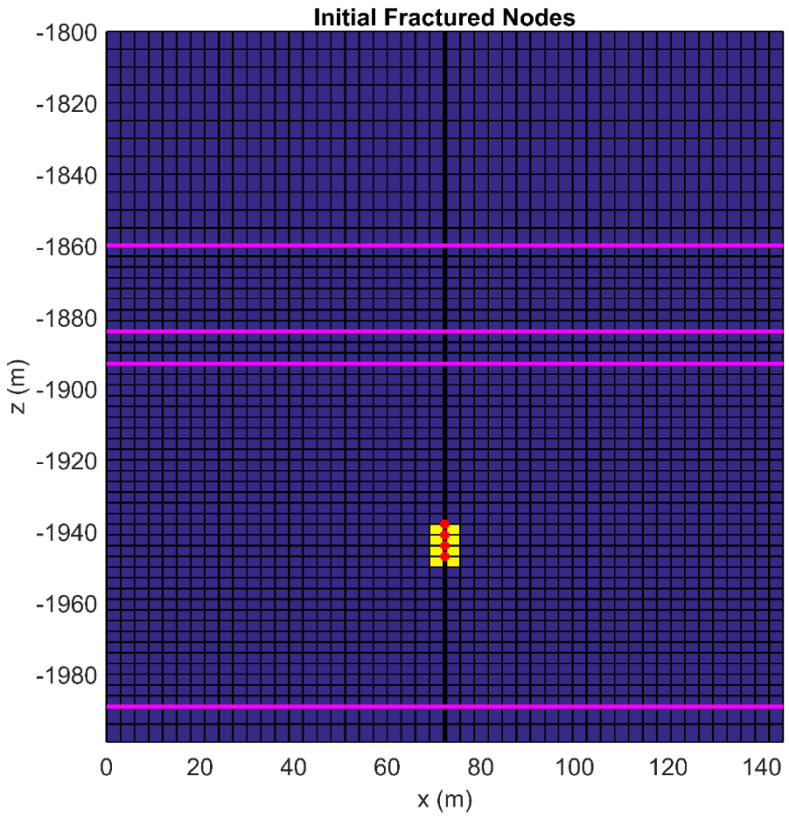

Figure 30. Initial fractured nodes and injection points

The fracture propagation is depicted below in a series of plots at different simulation times, shown in Figure 31**.** The fracture still only propagates within the Lower Barnett area for horizontal well.

Figure 32 shows that the pressure distribution stays below 50 MPa, and decreases in magnitude and increases in area as more water is injected. This is a result of the fracture gridblocks. As the pressure from water injection is divided among more fracture gridblocks, the pressure intensity decreases. This sharp contrast in pressure and area explains why the fracture propagation slows down as time goes on.

Figure 33 shows that the half fracture opening is mostly below 4 mm, with the maximum fracture opening occurring at later injection times. These openings translate into high permeabilities. The enhanced permeability delivers geomechanical loading from fluid injection to the areas away from the well. Also, the highest fracture openings occur at the injection points because of the increase pressure this area has when compared to the surrounding grids.

Unlike the pressure distribution, fracture aperture increases as injection time increases. On the first snapshot (when the injection time is 400 seconds) the fracture aperture reaches 3mm in contrast to the 4 mm of aperture at the latest snapshot (when the injection time is 2400 seconds).

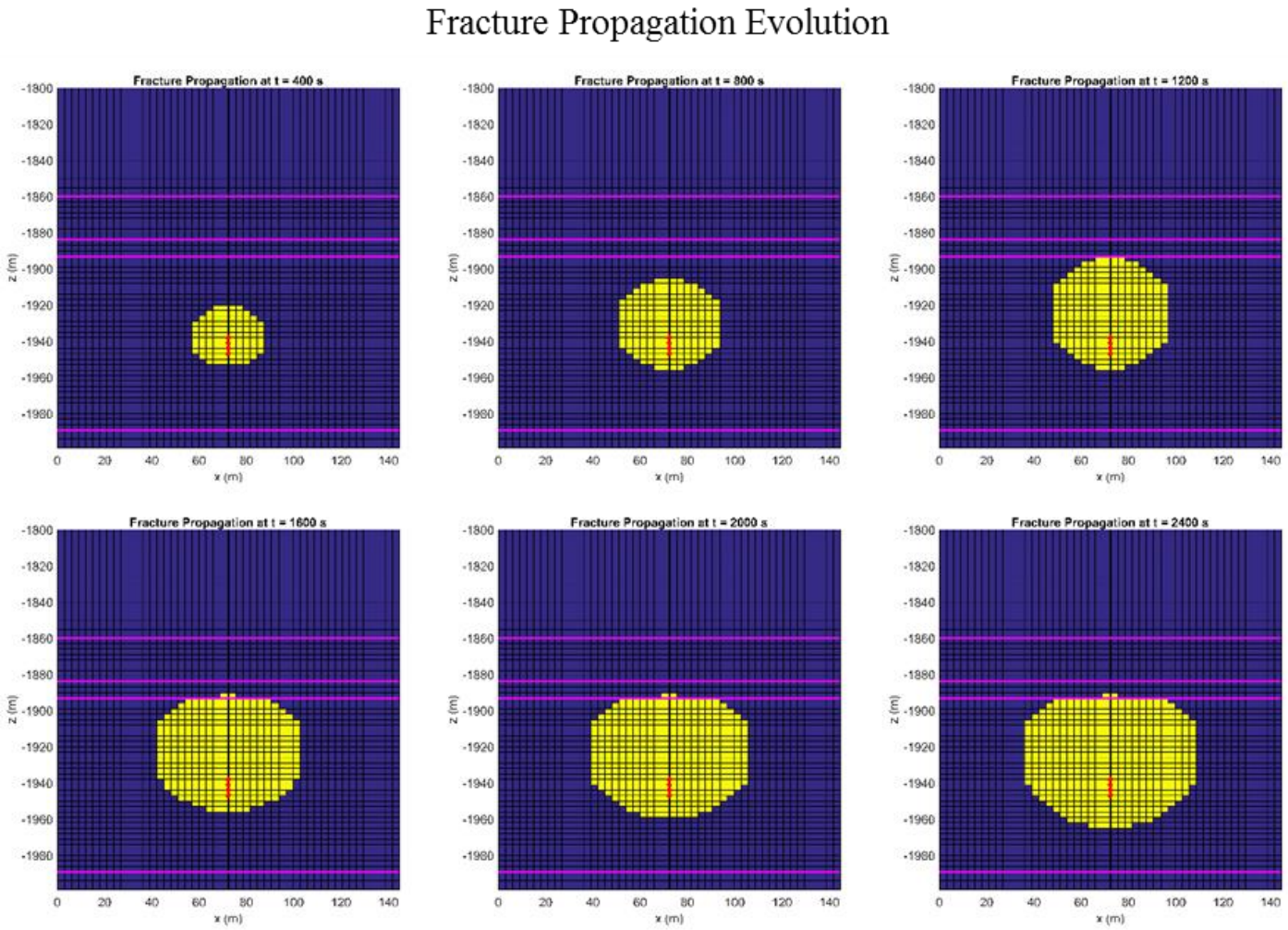

Figure 31. Fracture propagation at different times. Yellow blocks symbolize fracture nodes within a gridblock, while blue blocks represent intact rock gridblock.

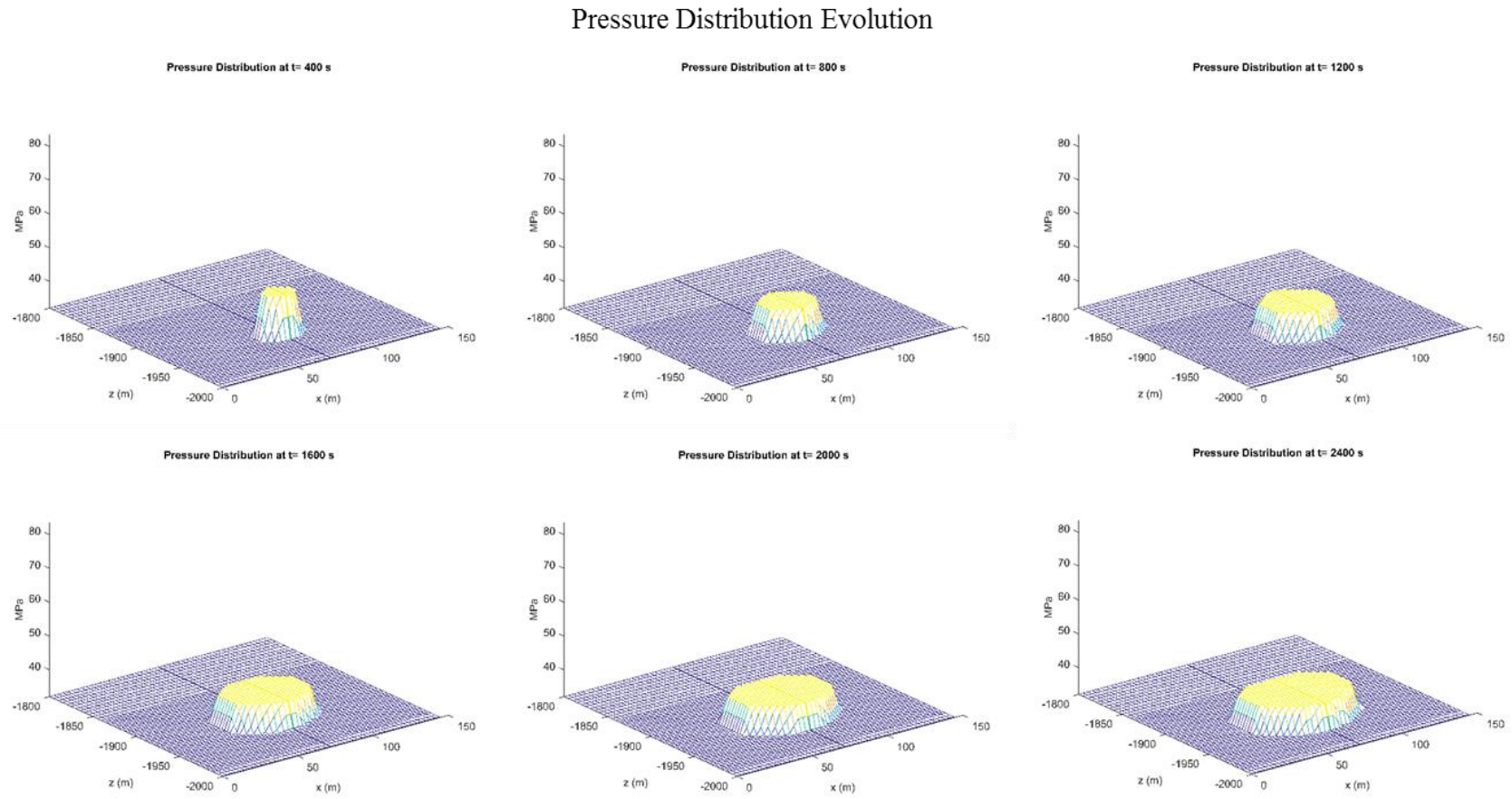

Figure 32. Pressure distribution evolution mesh.

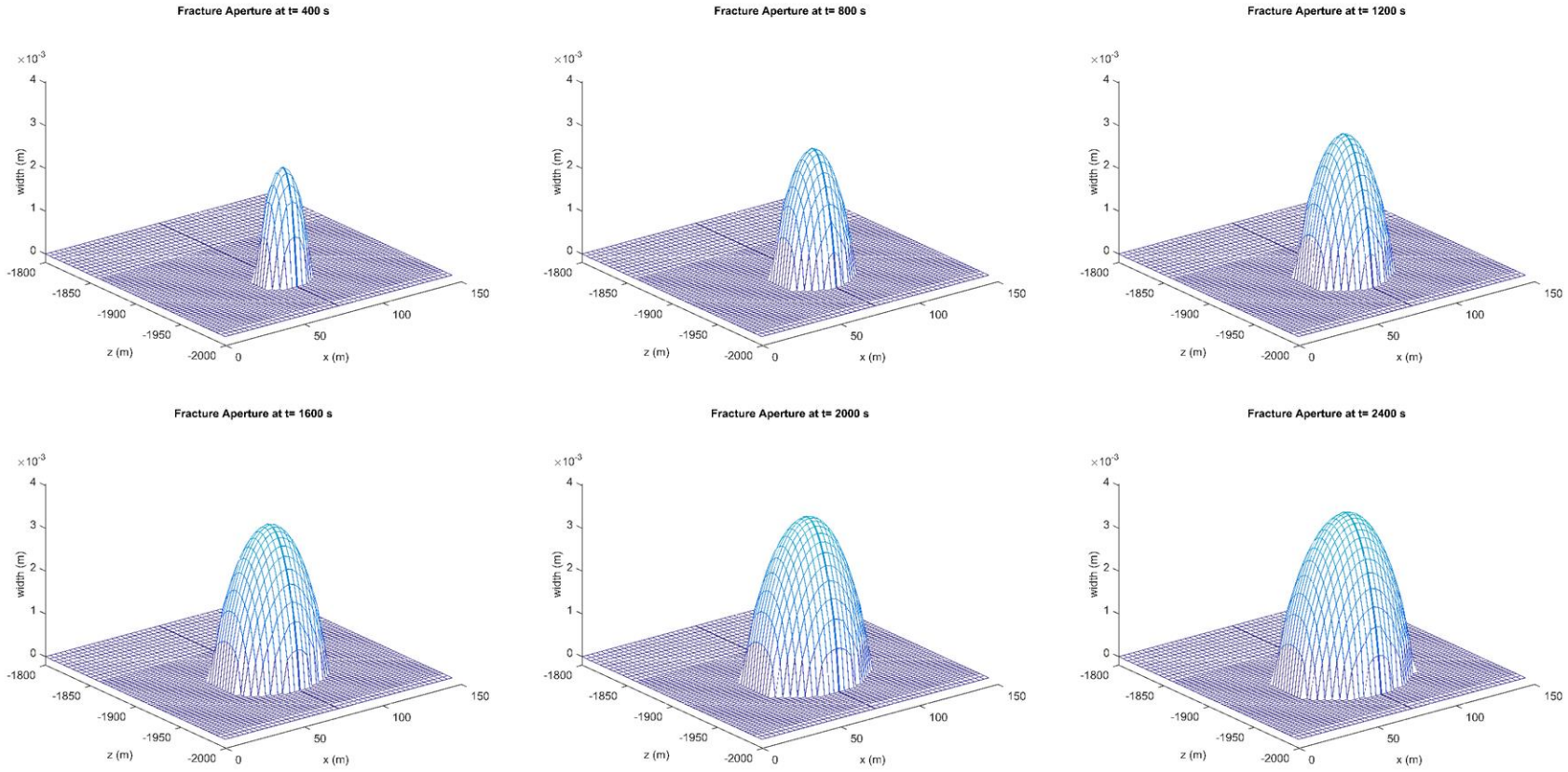

Figure 33. Fracture opening evolution mesh.

Figure 34 shows the total number of nodes fractured over the total simulation time, from which the propagation stability can be identified, and depicts stable fracture growth throughout the simulation time with the exception of a big jump around 400 seconds of injection time.

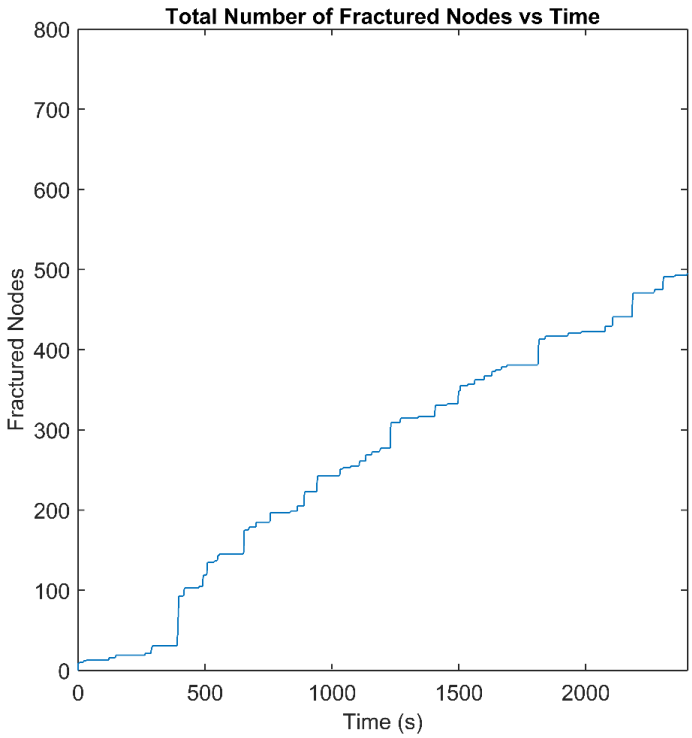

Figure 34. Fracture nodes vs time

The results of the modelling for micro-seismicity are shown in Figure 35-Figure 38. Location and moment magnitude (M_w) of MEQ's on z based on geomechanics solution, such as displacements and areas of fractured nodes. These MEQ events are tracked through time as the fracture propagation occurs, and by specific location in the

x-z plane to obtain a clear picture of how they relate to planar fracture propagation (i.e., 4 dimensional data).

From Figure 34, the moment magnitude (M_w) is, for the most part close to zero, which is well below safety concerns but it can still be recorded by a seismographer. From Figure 35-Figure 38. Location and moment magnitude (M_w) of MEQ's on z we can conclude that the MEQ locations again correspond to the fracture propagation.

Average	-0.2805
Range	0.2012 to -0.6975

Table 5. MEQ result summary for horizontal well simulation

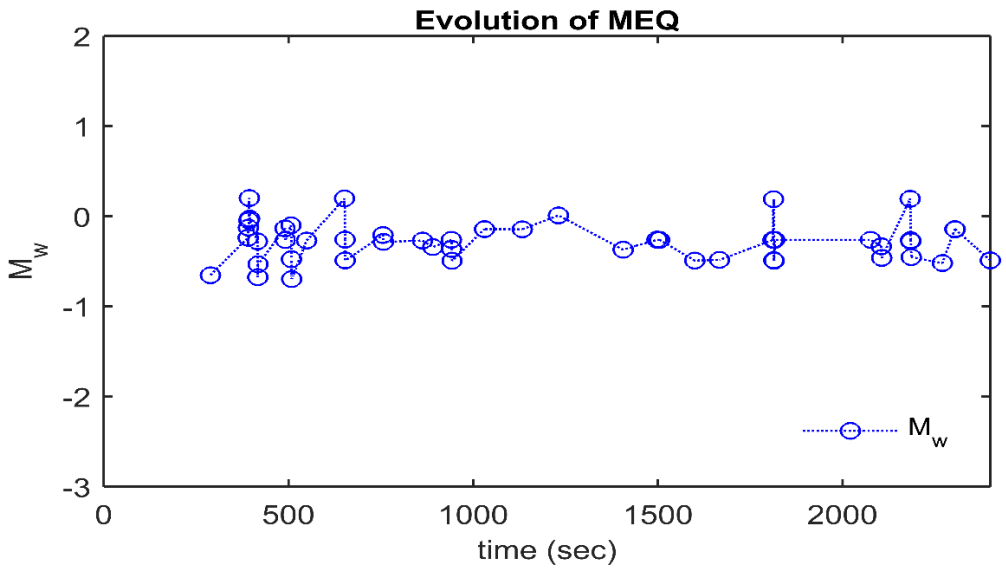

Figure 35. Evolution of moment magnitude (M_w) over time

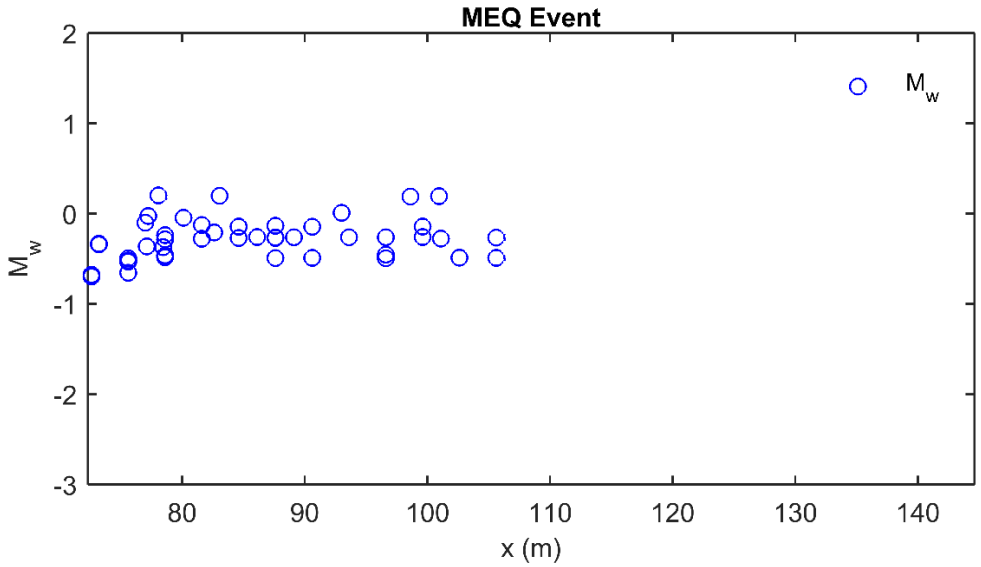

Figure 36. x-z location of MEQ's events (the right side of the fracture plane).

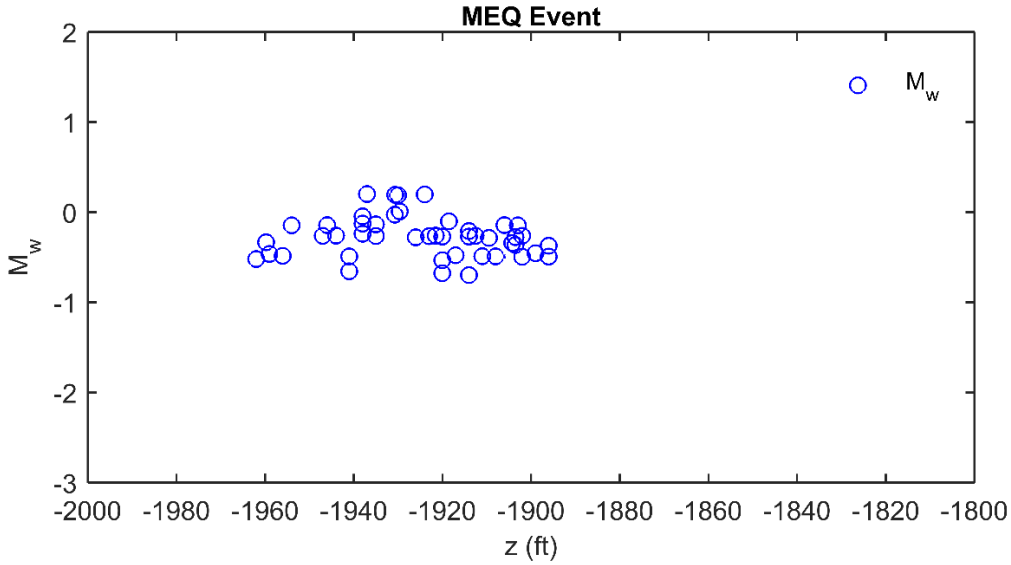

Figure 37. Location and moment magnitude (M_w) of MEQ's on x-direction (the right side of the fracture plane).

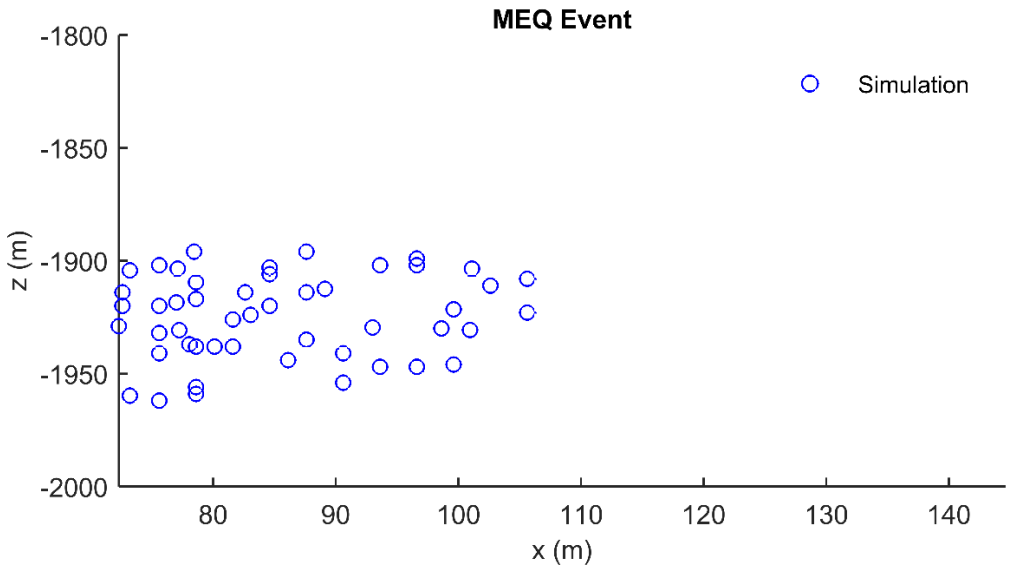

Figure 38. Location and moment magnitude (M_w) of MEQ's on z

4.2.2 Sensitivity Analysis of Simulator During Horizontal Fracturing

A coupled simulator requires large amounts of *a priori* information before been able to run simulations. The data gathering can take a substantial amount of time when the data quality is concerning or incomplete, so inputs often have to rely on correlations or extrapolations from different data sets. As a result, model calibration and initial setup takes multiple initial simulation runs and considerable time. Through the use of a sensitivity analysis of this section, this thesis seeks to study how the uncertainty of the model outputs can be apportioned to different sources of uncertainty in its inputs. The idea is that by performing a sensitivity analysis on the model, the relevance of each input can be assessed and the effort on the data collection can be properly allocated. Figure 39. Sensitivity analysis depiction. Inputs in green and output in red depicts the sensitivity analysis performed on the model. There were six sensitize inputs (Biot's coefficient,

Poisson's ratio, Young's modulus, injection rate, bulk density, tensile strength) and 2 sensitize outputs (Fracture nodes, MEQ Events)

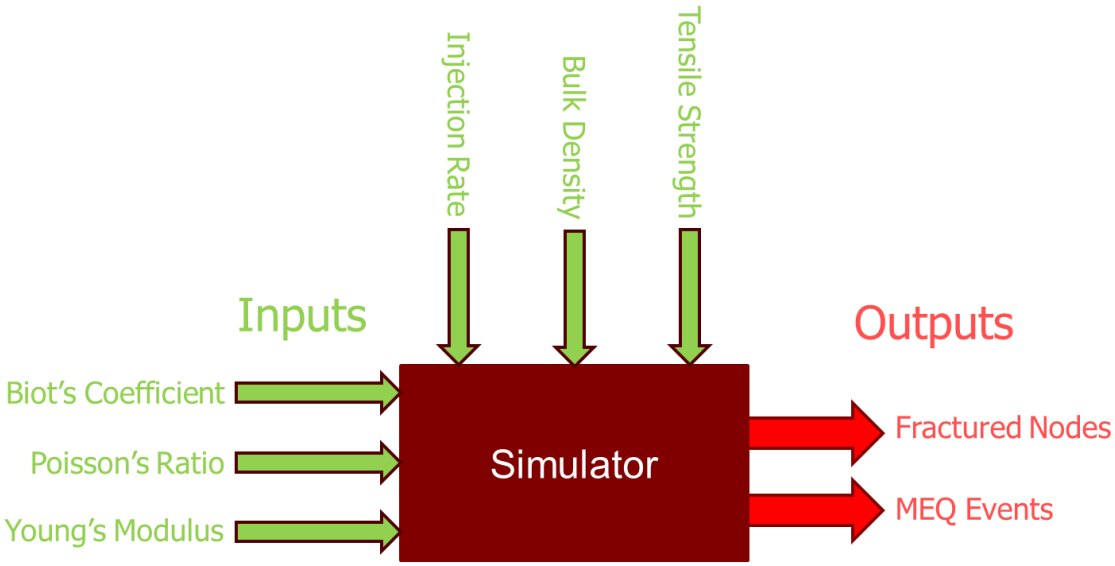

Figure 39. Sensitivity analysis depiction. Inputs in green and output in red

For this section, injection times were assumed to run through 2000 seconds. The cutoff time was determined based on the fracture propagation slowdown at larger simulation times.

Number of Fractured Nodes		
Series	80%	120%
Base	423	
Bulk Density	441	421
Tensile Strength	443	392
Youngs Modulus	355	489
Injection Rate	362	496
Poissons Ratio	675	310
Biots Coefficient	317	835

Table 6. Sensitivity analysis results for number of fractured nodes

In order to visualize the sensitivity results, a tornado plot (Figure 40) was created based on the results from Table 6 for the total number of fractured nodes. The tornado plot ranks the inputs in a simple visual manner to help identify the relative importance of the variables.

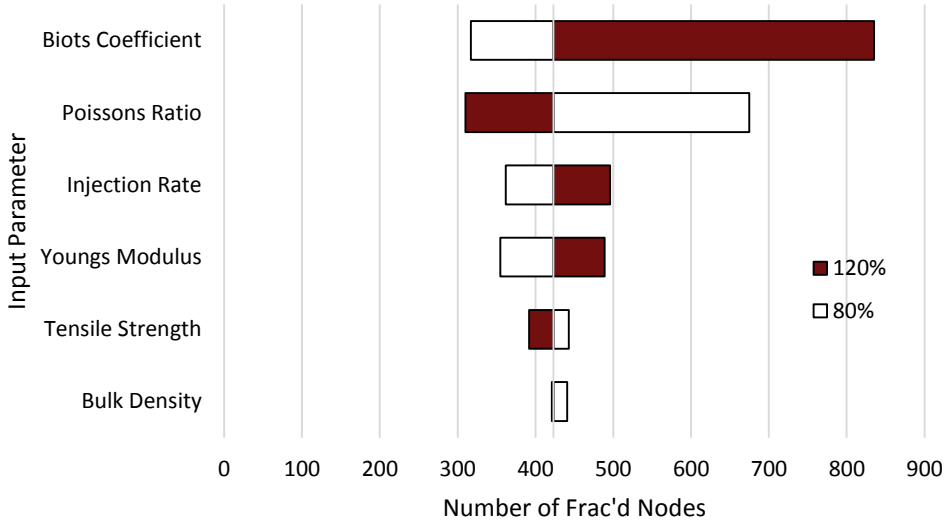

Figure 40. Tornado plot for number of fractured nodes sensitivity analysis

Similarly, a separate tornado plot (Figure 41) was created based on the results from Table 7 for the total number of micro-earthquakes generated. The tornado plot ranks the inputs in a simple visual manner to help identify the relative importance of the variables.

Number of MEQ Events		
Series	80%	120%
Base	80	
Bulk Density	86	80
Tensile Strength	90	78
Youngs Modulus	72	98
Injection Rate	72	108
Poissons Ratio	148	74
Biots Coefficient	54	192

Table 7. Sensitivity analysis results for number of MEQ events

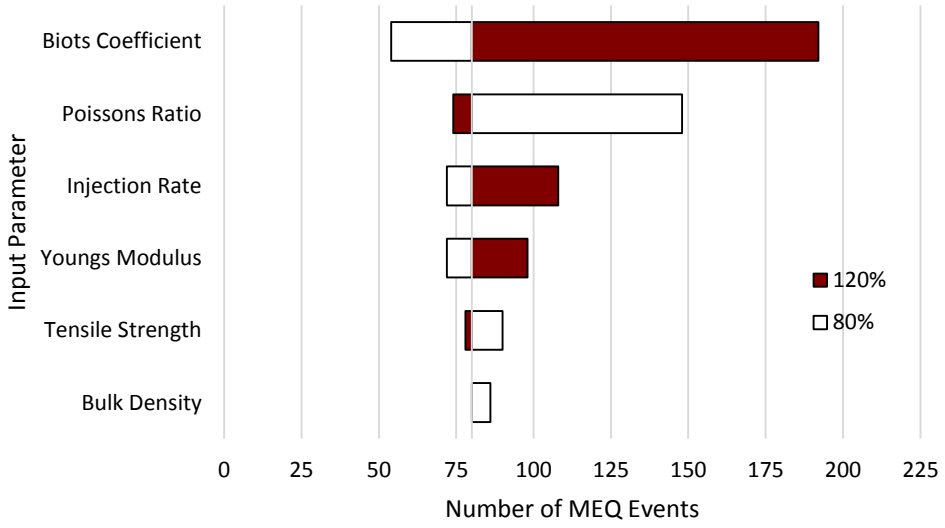

Figure 41. Tornado plot for number of MEQ events sensitivity analysis

From these two results we can observe that Biot's coefficient is the most influential input and it is calculated from experiments using equation 6. It is worth noting that both outputs ranked the input variables in the same order further reinforcing the notion that the coupling of flow, geomechanics, and MEQ is valid.

5. CONCLUSIONS

5.1 Fracture Propagation

1. For the Barnett Shale (i.e. pure normal faulting environment) the variations of horizontal minimum stress control the vertical growth of fractures as long as frac barriers are not present
2. Although failure or wellbore cement is possible under realistic operating conditions (faulty cement casing, high horizontal stress, etc.), the depth of shale reservoirs paired with rock heterogeneity limits the vertical extent of fractures generated
3. Vertical wells and fracturing stages near the heel of horizontal wells seem more at risk of unwanted fluid migration in the presence of poor cementing job

5.2 Micro-Earthquakes

1. The magnitudes of the simulated MEQs during hydraulic fracturing simulations are not large enough to warrant safety concerns unless faults exist
2. For all simulation cases, the event locations of MEQs correspond to the planar fracture propagation

5.3 Coupled Simulator

1. It is possible to couple a sequential flow-geomechanics simulator to model MEQs during hydraulic fracturing operations

2. It would be possible to history match reservoir properties using measured MEQ data and a forward coupled flow-geomechanics-MEQ geophysics simulator.
3. Uncertainty in the inputs controlled by operators does not seem to greatly change outputs of model

REFERENCES

Adachi, J., Siebrits, E., Peirce, A., & Desroches, J. (2007). Computer simulation of hydraulic fractures. International Journal of Rock Mechanics and Mining Sciences, 44(5), 739-757.

Aki, K., & Richards, P. G. (2002). Quantitative seismology (Vol. 1). Herndon: University Science Books.

Almon, W. R., Dawson, W. C., Ethridge, F. G., Rietsch, E., Sutton, S. J., & Castelblanco-Torres, B. (2005). Sedimentology and petrophysical character of Cretaceous Marine Shale sequences in foreland basins—Potential seismic response issues.

Arthur, J. D., Bohm, B. K., Coughlin, B. J., Layne, M. A., & Cornue, D. (2009, January). Evaluating the environmental implications of hydraulic fracturing in shale gas reservoirs. In SPE Americas E&P environmental and safety conference. Society of Petroleum Engineers.

Arthur, J. D., Bohm, B., & Layne, M. (2009). Hydraulic fracturing considerations for natural gas wells of the Marcellus Shale.

Aziz, K., & Settari, A. (1979). Petroleum reservoir simulation. London: Chapman & Hall.

Bear, J. (2013). Dynamics of fluids in porous media. North Chelmsford: Courier Corporation.

Berman, A. E., & Pittinger, L. F. (2011). US shale gas: less abundance, higher cost. The Oil Drum, 5(8), 12-36.

Bhandari, A. R., Flemings, P. B., Polito, P. J., Cronin, M. B., & Bryant, S. L. (2015). Anisotropy and stress dependence of permeability in the Barnett shale. Transport in Porous Media, 108(2), 393-411.

Biot, M. A. (1941). General theory of three-dimensional consolidation. Journal of applied physics, 12(2), 155-164.

Biot, M. A., & Willis, D. G. (1957). The elastic coefficients of the theory of consolidation. J. appl. Mech, 24, 594-601.

Bowker, K. A. (2007). Barnett Shale gas production, Fort Worth Basin: issues and discussion. AAPG bulletin, 91(4), 523-533.

Boyer, C., Kieschnick, J., Suarez-Rivera, R., Lewis, R. E., & Waters, G. (2006). Producing gas from its source. Oilfield Review, 18(3), 36-49.

Brooks, D. (2011, November 03). Shale Gas Revolution. Retrieved February 02, 2017, from http://www.nytimes.com/2011/11/04/opinion/brooks-the-shale-gas-revolution.html

Burgess, William J. "Geologic evolution of the Mid-Continent and Gulf Coast areas-A plate tectonics view." (1976).

Coussy, O. (1995). Mechanics of porous continua. Hoboken: John Wiley & Sons.

Coussy, O. (2004). Poromechanics. Hoboken: John Wiley & Sons.

Coussy, O., Eymard, R., & Lassabatere, T. (1998). Constitutive modelling of unsaturated drying deformable materials. Journal of Engineering Mechanics, 124(6), 658-667.

Dahm, T., & Krüger, F. (2014). Topic Moment tensor inversion and moment tensor interpretation.

De Pater, C. J., & Baisch, S. (2011). Geomechanical study of Bowland Shale seismicity. Synthesis Report, 57.

EIA, U. (2004). Assumptions for the Annual Energy Outlook 2004 With Projections to 2025.

EIA, US. "Annual energy outlook 2010." US Energy Information Administration, Washington, DC (2013): 60-62.

EIA. (n.d.). Trends in U.S. Oil and Natural Gas Upstream Costs. Retrieved February 02, 2017, from https://www.eia.gov/analysis/studies/drilling/

EPA. (2016, September 06). Class II Oil and Gas Related Injection Wells. Retrieved February 06, 2017, from https://www.epa.gov/uic/class-ii-oil-and-gas-related-injection-wells

Eshkalak, M. O., Mohaghegh, S. D., & Esmaili, S. (2014). Geomechanical properties of unconventional shale reservoirs. Journal of Petroleum Engineering, 2014.

Fisher, M. K., Wright, C. A., Davidson, B. M., Goodwin, A. K., Fielder, E. O., Buckler, W. S., & Steinsberger, N. P. (2002, January). Integrating fracture mapping technologies to optimize stimulations in the Barnett Shale. In SPE Annual Technical Conference and Exhibition. Society of Petroleum Engineers.

Fry, M., Hoeinghaus, D. J., Ponette-González, A. G., Thompson, R., & La Point, T. W. (2012). Fracking vs faucets: balancing energy needs and water sustainability at urban frontiers.

Geertsma, J. (1957). A remark on the analogy between thermoelasticity and the elasticity of saturated porous media. Journal of the Mechanics and Physics of Solids, 6(1), 13-16.

Hargrove, U., Adams, C., Berend, B., Grace, M., & Mullen, M. (2015, July). The Marble Falls Fractured Resource Play: Unconventional Technology Turns An Old Trend Into The Next Big Play. In Unconventional Resources Technology Conference, San Antonio, Texas, 20-22 July 2015 (pp. 769-776). Society of Exploration Geophysicists, American Association of Petroleum Geologists, Society of Petroleum Engineers.

Holland, A. A. (2013). Earthquakes triggered by hydraulic fracturing in south-central Oklahoma. Bulletin of the Seismological Society of America, 103(3), 1784-1792.

Hsieh, P. A., & Bredehoeft, J. D. (1981). A reservoir analysis of the Denver earthquakes: A case of induced seismicity. Journal of Geophysical Research: Solid Earth, 86(B2), 903-920.

Jost, M. U., & Herrmann, R. B. (1989). A student's guide to and review of moment tensors. Seismological Research Letters, 60(2), 37-57.

Kanamori, H. (1977). The energy release in great earthquakes. Journal of geophysical research, 82(20), 2981-2987.

Kim, J. (2010). Sequential methods for coupled geomechanics and multiphase flow (Doctoral dissertation, Stanford University).

Kim, J., & Moridis, G. J. (2013). Development of the T+ M coupled flow–geomechanical simulator to describe fracture propagation and coupled flow–

thermal–geomechanical processes in tight/shale gas systems. Computers & Geosciences, 60, 184-198.

Kim, J., Moridis, G. J., & Martinez, E. R. (2016). Investigation of possible wellbore cement failures during hydraulic fracturing operations. Journal of Petroleum Science and Engineering, 139, 254-263.

Kim, J., Tchelepi, H. A., & Juanes, R. (2011). Stability and convergence of sequential methods for coupled flow and geomechanics: Fixed-stress and fixed-strain splits. Computer Methods in Applied Mechanics and Engineering, 200(13), 1591-1606.

King, R. F., & Morehouse, D. (1993). Drilling sideways—a review of horizontal well technology and its domestic application. Energy Information Administration Technical Report.

Kostrov, V. V. (1974). Seismic moment and energy of earthquakes, and seismic flow of rock. Izv. Acad. Sci. USSR Phys. Solid Earth, 1, 23-44.

Loucks, R. G., & Ruppel, S. C. (2007). Mississippian Barnett Shale: Lithofacies and depositional setting of a deep-water shale-gas succession in the Fort Worth Basin, Texas. AAPG bulletin, 91(4), 579-601.

Malewitz, J. (2014, December 15). Dissecting Denton: How One City Banned Fracking. Retrieved February 06, 2017, from https://www.texastribune.org/2014/12/15/dissecting-denton-how-texas-city-baned-fracking/

Marinos, P., & Hoek, E. (2000, November). GSI: a geologically friendly tool for rock mass strength estimation. In ISRM International Symposium. International Society for Rock Mechanics.

Martineau, D. F. (2007). History of the Newark East field and the Barnett Shale as a gas reservoir. AAPG bulletin, 91(4), 399-403.

Martinez Rodriguez, E., Kim, J., & Moridis, G. J. (2016, June). Numerical Modelling of Microearthquakes by Using Coupled Geomechanics Simulation for Planar Fracture Propagation. In 50th US Rock Mechanics/Geomechanics Symposium. American Rock Mechanics Association.

Maxwell, S. C., et al. "Fault activation during hydraulic fracturing." SEG Technical Program Expanded Abstracts 2009. Society of Exploration Geophysicists, 2009. 1552-1556.

McClure, M., Gibson, R., Chiu, K., & Ranganath, R. (2016). Identifying potentially induced seismicity and assessing statistical significance in Oklahoma and California. arXiv preprint arXiv:1611.03414.

McGlade, C., Speirs, J., & Sorrell, S. (2013). Unconventional gas–a review of regional and global resource estimates. Energy, 55, 571-584.

Montgomery, S. L., Jarvie, D. M., Bowker, K. A., & Pollastro, R. M. (2005). Mississippian Barnett Shale, Fort Worth basin, north-central Texas: Gas-shale play with multi–trillion cubic foot potential. AAPG bulletin, 89(2), 155-175.

New Mexico and fracking. (n.d.). Retrieved February 02, 2017, from http://www.sourcewatch.org/index.php/New_Mexico_and_fracking

New, Rigorous Assessment of Shale Gas Reserves Forecasts Reliable Supply from Barnett Shale Through 2030. (2013, February 28). Retrieved February 02, 2017, from http://news.utexas.edu/2013/02/28/new-rigorous-assessment-of-shale-gas-reserves-forecasts-reliable-supply-from-barnett-shale-through-2030

Newman, G. H. (1973). Pore-volume compressibility of consolidated, friable, and unconsolidated reservoir rocks under hydrostatic loading. Journal of Petroleum Technology, 25(02), 129-134.

Nolte, K. G., & Economides, M. J. (1989). Fracturing diagnosis using pressure analysis.

Perez, R., & Marfurt, K. (2013, September). Calibration of brittleness to elastic rock properties via mineralogy logs in unconventional reservoirs. In AAPG International Conference and Exhibition (Vol. 41237). American Association of Petroleum Geologists Cartagena, Colombia.

Perryman Report: Barnett Shale (n.d.). Retrieved February 02, 2017, from https://www.perrymangroup.com/special-reports/the-economic-and-fiscal-contribution-of-the-barnett-shale/

Pollastro, R. M., Hill, R. J., Jarvie, D. M., & Henry, M. E. (2003). Assessing undiscovered resources of the Barnett-Paleozoic total petroleum system, Bend Arch-Fort Worth basin province, Texas.

Pollastro, R. M., Jarvie, D. M., Hill, R. J., & Adams, C. W. (2007). Geologic framework of the Mississippian Barnett Shale, Barnett-Paleozoic total petroleum system, Bend archFort Worth Basin, Texas. AAPG bulletin, 91(4), 405-436.

Railroad Commission. (n.d.). Retrieved February 02, 2017, from http://www.rrc.state.tx.us/oil-gas/major-oil-gas-formations/barnett-shale-information/

Richter, C. F. (1935). An instrumental earthquake magnitude scale. Bulletin of the Seismological Society of America, 25(1), 1-32.

Rogers, H. (2011, March 01). Shale gas-the unfolding story. Retrieved February 02, 2017, from https://doi.org/10.1093/oxrep/grr004

Rozhko, A. Y. (2010). Role of seepage forces on seismicity triggering. Journal of Geophysical Research: Solid Earth, 115(B11).

Senftle, J. T., & Landis, C. R. (1991). Vitrinite reflectance as a tool to assess thermal maturity. Source and migration processes and evaluation techniques: AAPG Treatise of Petroleum Geology, Handbook of Petroleum Geology, 119-125.

Settari, A., & Mourits, F. M. (1998). A coupled reservoir and geomechanical simulation system. Spe Journal, 3(03), 219-226.

Solutions, C. Long-Term Integrity of Deepwater Cement Systems Under Stress/Compaction Conditions. MMS Project, Report, 3.

Stevens, P. (n.d.). The 'Shale Gas Revolution': Developments and Changes. Retrieved February 02, 2017, from https://www.chathamhouse.org/publications/papers/view/185311

Thrasher, M. (2016, November 14). Oklahoma Insurance Regulators Still Face An Unprecedented Risk. Retrieved February 06, 2017, from

http://www.forbes.com/sites/michaelthrasher/2016/07/28/oklahoma-insurance-regulators-still-face-an-unprecedented-risk/#7c68e7101553

Tian, Y., & Ayers, W. B. (2010, January). Barnett Shale (Mississippian), Fort Worth Basin, Texas: regional variations in gas and oil production and reservoir properties. In Canadian Unconventional Resources and International Petroleum Conference. Society of Petroleum Engineers.

Veatch Jr, R. W., & Moschovidis, Z. A. (1986, January). An overview of recent advances in hydraulic fracturing technology. In International Meeting on Petroleum Engineering. Society of Petroleum Engineers.

Verdon, J. P., Kendall, J. M., & Maxwell, S. C. (2010). A comparison of passive seismic monitoring of fracture stimulation from water and CO 2 injection. Geophysics, 75(3), MA1-MA7.

Vermylen, J. P., Zoback, M. D., Beroza, G. C., & Kovscek, A. R. (2011). Geomechanical studies of the Barnett shale, Texas, USA. Stanford University.

Vermylen, J., & Zoback, M. D. (2011, January). Hydraulic fracturing, microseismic magnitudes, and stress evolution in the Barnett Shale, Texas, USA. In SPE Hydraulic Fracturing Technology Conference. Society of Petroleum Engineers.

Wang, Q., Chen, X., Jha, A. N., & Rogers, H. (2014). Natural gas from shale formation–the evolution, evidences and challenges of shale gas revolution in United States. Renewable and Sustainable Energy Reviews, 30, 1-28.

Wang, X., Wang, L. B., & Xu, L. M. (2004). Formulation of the return mapping algorithm for elastoplastic soil models. Computers and Geotechnics, 31(4), 315-338.

Warpinski, N. (2009). Microseismic monitoring: Inside and out. Journal of Petroleum Technology, 61(11), 80-85.

Willis, J. (2014, September 09). Shale 101 - More Evidence of the Power of Shale. Retrieved February 02, 2017, from http://naturalgasnow.org/shale-101-evidence-power-shale/

Witherspoon, P. A., Wang, J. S., Iwai, K., & Gale, J. E. (1980). Validity of cubic law for fluid flow in a deformable rock fracture. Water resources research, 16(6), 1016-1024.

Zhao, H., Givens, N. B., & Curtis, B. (2007). Thermal maturity of the Barnett Shale determined from well-log analysis. AAPG bulletin, 91(4), 535-549.

Zoback, M., Kitasei, S., & Copithorne, B. (2010). Addressing the environmental risks from shale gas development (Vol. 21). Washington, DC: Worldwatch Institute.